https://doi.org/10.5194/egusphere-2024-771
Preprint. Discussion started: 22 April 2024

Simulation of cold powder avalanches considering daily snowpack and weather situations to enhance road safety

Julia Glaus[1,2], Katreen Wikstrom Jones[3], Perry Bartelt[1,2], Marc Christen[1,2], Lukas Stoffel[1], Johan Gaume[1,2,4], and Yves Bühler[1,2]

[1]WSL Institute for Snow and Avalanche Research SLF, Davos Dorf, 7260 Switzerland
[2]Climate Change, Extremes, and Natural Hazards in Alpine Regions Research Centre CERC, Davos Dorf, 7260 Switzerland
[3]Alaska Division of Geological & Geophysical Surveys, Anchorage
[4]Institute for Geotechnical Engineering, ETH Zurich, Zurich, 8057 Switzerland

Correspondence: Julia Glaus (julia.glaus@slf.ch)

Abstract. Snow avalanches are rapid gravitational mass movements that represent a significant hazard to both humans and infrastructure, including traffic lines. In this context, risk management in mountainous region usually relies on experience of avalanche experts, observations in the field, weather and snowpack measurements and numerical simulations, which are typically based on shallow water equations.

Ensuring road safety requires considering daily weather conditions, snowpack characteristics, and terrain features. To include a numerical model in the decision process for road safety, it is essential to incorporate these aspects and provide insights into utilising measurements as input parameters for the simulations.

This study investigates the predictive capabilities of the numerical simulation model RAMMS::EXTENDED, an extended version of the well established RAMMS software developed at the WSL Institute for Snow and Avalanche research SLF over the past fifteen years, to estimate avalanche run-out distances. Specifically tailored to cold powder avalanches dynamics, taking into account the temperature of the snowpack and erosion, our inquiry utilises meteorological station measurements as an input to evaluate the model's performance.

We begin by providing an overview of the model, examining its physical and practical aspects. We then conduct a sensitivity analysis on input and system parameters, focusing on avalanche dynamics representation. Leveraging drone-based observational data, we perform a comparative analysis to validate the simulation results.

Additional to the recalculation of avalanches due to the sensitivity analysis, we show that we achieve meaningful predictions of the avalanche run-out distance for cold powder avalanches incorporating snow height and snow temperature measured by weather stations at two different altitudes. In the future, a further refined and validated version of this approach could allow for near real time hazard assessments to improve the decision making for road-closer and re-opening. Additionally, we plan to calibrate the model for wet-snow avalanches, to cover a larger range of weather and snowpack scenarios.

https://doi.org/10.5194/egusphere-2024-771
Preprint. Discussion started: 22 April 2024

Figure 1. Pictures from avalanche on the I-90 road at the Snoqualmie pass. The interruption of a traffic line not only impacts transportation but disrupts crucial lifelines, hindering workers from reaching their workplaces. To underscore the economic consequences, the temporary closure of I-90, a vital link connecting the eastern and western coasts of the U.S., resulted in an estimated overall economic loss of 27 million USD and the loss of 170 jobs (John, 2012). Incorporating numerical simulation results into the decision-making process for such a road can significantly reduce closure times, enhance safety, and mitigate economic consequences on a global scale (source: https://www.flickr.com/photos/wsdot/2252548089).

1 Introduction

In this paper, our aim is to provide a tool to enhance road safety in avalanche-prone terrain by integrating drone technology and snow measurements into numerical modelling techniques. Due to economic and environmental constraints, many mountain roads cannot be effectively protected using long-term technical measures to prevent avalanche release (avalanche defence structures) or inundation (road alignment, snow sheds and tunnels). Therefore local hazard experts must make decisions to close roads and stop all traffic during avalanching periods (Fig. 1). These decisions rely on information from the warning services, the interpretation of measurement data and experience (Stoffel and Schweizer, 2008). Increasingly computer-based expert systems such as the nearest-neighbour model for regional avalanche forecasting called NXD (Brabec and Meister, 2001) or AI systems are applied to help the hazard experts.

In this work, we focus on adding information to the decision-making process by combining data from weather stations, drone measurements and numerical modelling. The primary goal is to answer the question whether an avalanche could reach a road under specific snowpack and weather conditions. Having this information at hand could enhance road safety mitigation and reduce the road closure times to a minimum. For this approach to be successful and to include all possible avalanche paths along a road, accurate reports of snowpack and weather conditions are needed. This data must be collected as close as possible to the specific avalanche path.

https://doi.org/10.5194/egusphere-2024-771
Preprint. Discussion started: 22 April 2024

The utilisation of numerical avalanche dynamics modelling to enhance road safety signifies an important paradigm shift in avalanche engineering. While numerical models have traditionally and extensively been adopted for generating hazard maps and designing avalanche defence structures along specific avalanche paths, they often don't include crucial snow properties such as snow cover layering, density, temperature, or moisture content. Avalanche fracture heights are typically determined through statistical analysis of long-term snow accumulation data from measurement stations (Salm et al., 1990). Following an approach pioneered by Voellmy (Voellmy, 1955) extreme avalanche events are typically addressed using calibrated parameters derived from historical avalanche occurrences (Gruber and Bartelt, 2007). While this approach is suitable for hazard mapping, it fails to leverage recent advancements in automatic weather stations or drone measurements (Bühler et al., 2017). Consequently, the output from numerical models available to local hazard engineers for deciding whether to close a road is limited, as it becomes challenging to correlate specific measured data with potential avalanche run-outs. A first system using numerical simulations for road safety is implemented in Chile as described in (Valero et al., 2017). It uses avalanche dynamic modelling based on RAMMS to predict whether an avalanche reaches a road. For the input data it relies additionally on the simulation tool snowpack (Cerda et al., 2016; Lehning et al., 1999).

The problem of road safety therefore places new demands on existing numerical models. To accurately represent snow and weather conditions, a model must have the capability to encompass avalanches with different flow regimes, (including wet-, mixed- and dry snow avalanches), consider snowcover entrainment and mass growth, the braking effects of different forest compositions and, most importantly, the influence of snow temperature. Existing avalanche dynamics models which focus on the flowing regime, ELBA (Keiler et al., 2006), OpenFOAM (Rauter et al., 2018), r.avaflow (ava, 2023) and RAMMS::Avalanche (Christen et al., 2010) only fulfil partially those requirements.

In this paper, we utilise three well-documented avalanches that cut a mountain road near Davos (Switzerland) to invest the limitations of using avalanche dynamics models with weather station data. The avalanches were artificially released and developed into a mixed flowing powder type. Post-event drone scans provided detailed information of run-out and snowcover distribution. We apply an extended RAMMS model that includes snow temperature (Vera Valero et al., 2016), entrainment (Bartelt et al., 2018a) and formation and propagation of the powder cloud (Zhuang et al., 2023a). The observed avalanches are back-calculated using temperature data from nearby snow monitoring stations. We show how the model reacts to changing boundary conditions and the sensitivity of model performance on variation of parameters. Our results highlight the challenges of using avalanche dynamics models for road safety applications.

2 Observations and Methods

2.1 Avalanche events, Davos, January 16, 2019

We examine three separate avalanche events that took place in the vicinity of Davos, Switzerland. These incidents occurred in mid-January 2019 in the Dischma valley during a cold weather period, leading to the formation of mixed flowing-powder avalanches, see Fig. 2. The three avalanche tracks are located near the Braemabuehl region of Davos and have the names *Wildi*, *Ruechi* and *Chaiseren* (Fig. 3). The release zones are all located at roughly 2300 m.a.s.l on a northern aspect. The tracks drop

https://doi.org/10.5194/egusphere-2024-771
Preprint. Discussion started: 22 April 2024

(a) Deposition of Wildi, Ruechi and Chaisere avalanche after the snow storm.

(b) Ruechi avalanche run down on the Dischma road in a side valley of Davos. The powder cloud continues till the counter slope.

Figure 2. Powder avalanches in the Dischma valley, Davos Switzerland. These avalanches originated from northern slopes. Powder avalanches often reach the valley road after traversing a short, level run-out zone (Pictures made by Vali Meier, SOS Davos Klosters).

between 650 m and 750 m in elevation running over a well-used cross country skiing track and a road. The tracks are somewhat channelised below the release zone, but open to wide, laterally unconstrained, run-out zones at the valley bottom. In the past, avalanches from these tracks have blocked the road connecting the inhabitants of the valley and Davos, wood constructions have been destroyed and trees in the surrounding forests have been blown-over by avalanche air-blasts. For all three tracks hazard maps exist.

The 2019 avalanche events are unique since substantial snowfall preceded the cold spell, with snow depths as high as 2.5m measured at nearby snowcover monitoring stations. A strong winter storm passed through the valley on the 14.01.2019 with strong winds which redistributed snow on the slope. The avalanches eroded a deep snowpack, which coupled with cold snow temperatures, contributed to the formation of powder avalanches. The avalanches were artificially released and additional pictures from the helicopter during the controlled avalanche mitigation provided insights into the avalanche speed and powder cloud height. The avalanches considerably increased in mass after release due to snow entrainment. In the following days, a field campaign was initiated by the institute for snow and avalanche (SLF) to gather data concerning the location of the release zones, erosion heights and avalanche run-out lengths. The data was coupled with temperature data from nearby snow monitoring stations (Weissfluhjoch and IMIS SLF2) which are situated 6 km and 3 km away. The Weissfluhjoch station is located at the same elevation as the avalanche release zones (2300 m.a.s.l) and the IMIS SLF2 at the same elevation as the run-out zones (1570 m.a.s.l).

On-site data collection was conducted with structure-from-motion photogrammetry (Bühler et al., 2011) using drones, allowing the measurement of snow heights by comparing post-avalanche elevation surfaces with bare ground surfaces during the summer obtained from the Federal Swiss topographical survey (SwissTopo) (Swisstopo). In Fig. 4, the measured post-

https://doi.org/10.5194/egusphere-2024-771
Preprint. Discussion started: 22 April 2024

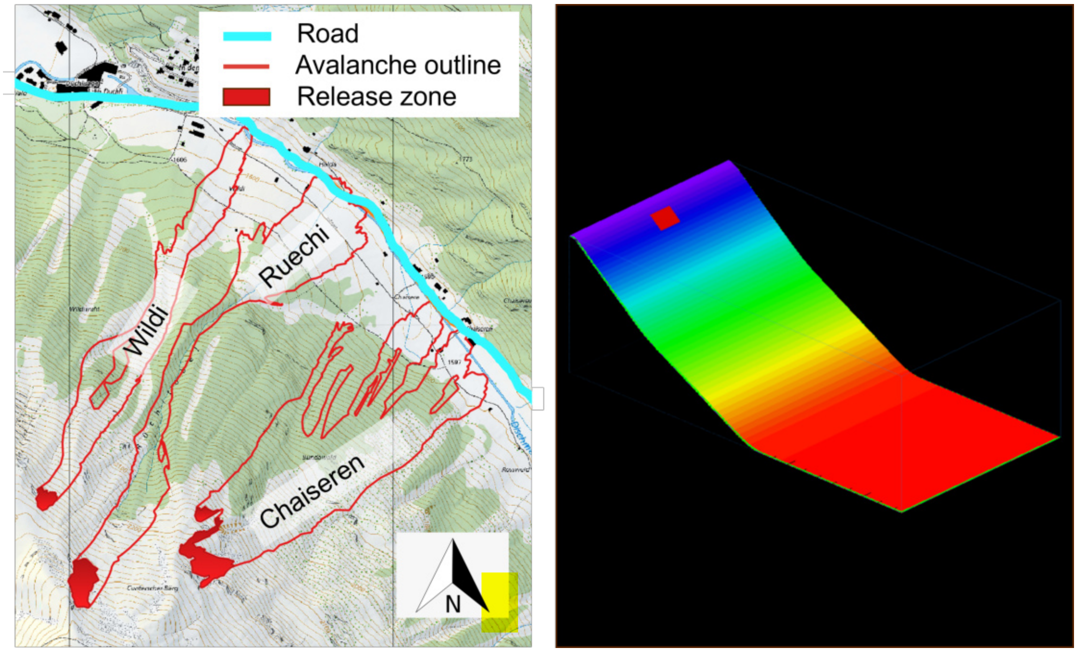

Figure 3. On the left side, depiction of release zone and measured outline of the three avalanches at Braemabuehl on January 16, 2019. The artificially released avalanche crossed the road. On the right pictures, the idealised planar slope to represent the steepness of Ruechi (map source: Federal Office of Topography).

avalanche snow heights for all three avalanche tracks are shown. This drone data allowed the delineation of the release zones, thanks to a clearly visible stauchwall. Avalanche fracture height (d_0) could be estimated by comparing measured snow heights at similar altitudes to the average snow height in the release zone after avalanche release. Additionally, from the drone measurements the snow distribution gradient ΔD could be determined. These values are reported as the average decrease in snowcover height per 100 m drop in elevation (Fig. 6).

To better understand temperature gradients ΔT (Fig. 6), we analysed snow pits concurrently with temperature readings at Weissfluhjoch and SLF stations (Attachment A1). The average temperature of the released snowpack was used to infer temperature gradients and snow density in the release zone, further interpolated across stations at varying altitudes to understand snow cover gradients.

Our approach was to simulate the avalanche events from 2019 based on meteorological data and validate the results to the avalanche outlines and dimensions that we measured based on the post-avalanche drone data. We started by simulating one avalanche and then apply the parameter set of this avalanche to the other two tracks as they were triggered almost at the same time and hence should have the same input data. A summary of the snowcover and temperature input data of the Braemabuel events is presented in Table 1. The same avalanching period in January 2019 produced a well-documented event on the nearby Salezer avalanche track in Davos (a day earlier) as well as a powder avalanche at the experimental Vallée de la Sionne test

https://doi.org/10.5194/egusphere-2024-771
Preprint. Discussion started: 22 April 2024

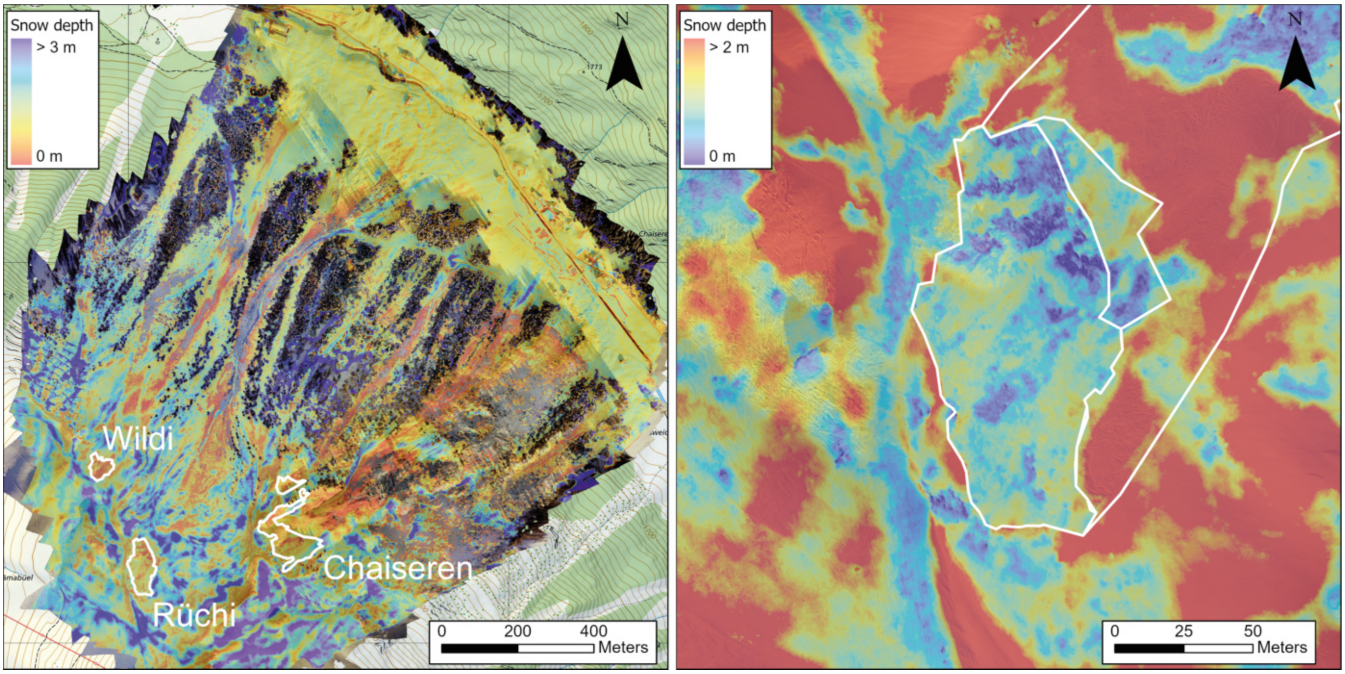

Figure 4. Snow depth distribution mapped photogrammetrically with the eBee RTK drone on 16 January 2019 for the entire area (left) and zoomed to the Ruechi avalanche release zone (right) after the avalanches got triggered. Significant wind redistribution effects are visible in the image (map source: Federal Office of Topography).

site (Ammann, 1999) which we could additionally use for validation. In this publication we keep the focus on the Braemabuel event to describe our methodology.

2.2 Evaluation Approach

For road safety problems, our focus lies on evaluating if an avalanche can reach the road, and if so, what length of road is covered by the avalanche. In a further step, the pressure of the powder cloud and the velocity of the core must be included in the evaluation process. This involves estimating the extent of both the core and cloud impact pressures. For this purpose we have developed a post-processing tool to assess model outputs based on the maximum values of velocity, flow height, and pressure per calculation cell as described in (Glaus et al.). We extract the outlines of both the core and cloud, determining the longest distance by identifying the two most distant points. For core outline we identify pixels with a flow height greater than 0.1 m and a velocity less than 1 m/s. For the cloud, the outline is based on pressure with a minimum threshold set at 0.5 kPa. While this method works well for simple avalanches, it requires careful consideration in cases where avalanches exhibit finger formation or the avalanche strongly deviates in the lateral direction. For all avalanche simulations, a grid resolution of 5 m is chosen.

https://doi.org/10.5194/egusphere-2024-771
Preprint. Discussion started: 22 April 2024

Table 1. Overview of the measured snow height and temperature data for the Braemabuel events.

Snow cover disposition	**Wildi**	**Ruechi**	**Chaiseren**
Release height d_0	0.95 m	1.45 m	0.95 m
Release density ρ_0	200 kg/m^3	200 kg/m^3	200 kg/m^3
Erosion height d_0^*	1.15 m	1.85 m	1.15 m
Erosion gradient ΔD	0.1 m/100m	0.1 m/100m	0.1 m/100m
Erosion density ρ_Σ	193 kg/m^3	193 kg/m^3	193 kg/m^3
Release temperature T	-8.1 °C	-8.4 °C	-7.8 °C
Temperature gradient ΔT	0.5 °C/100m	0.5 °C/100m	0.5 °C/100m

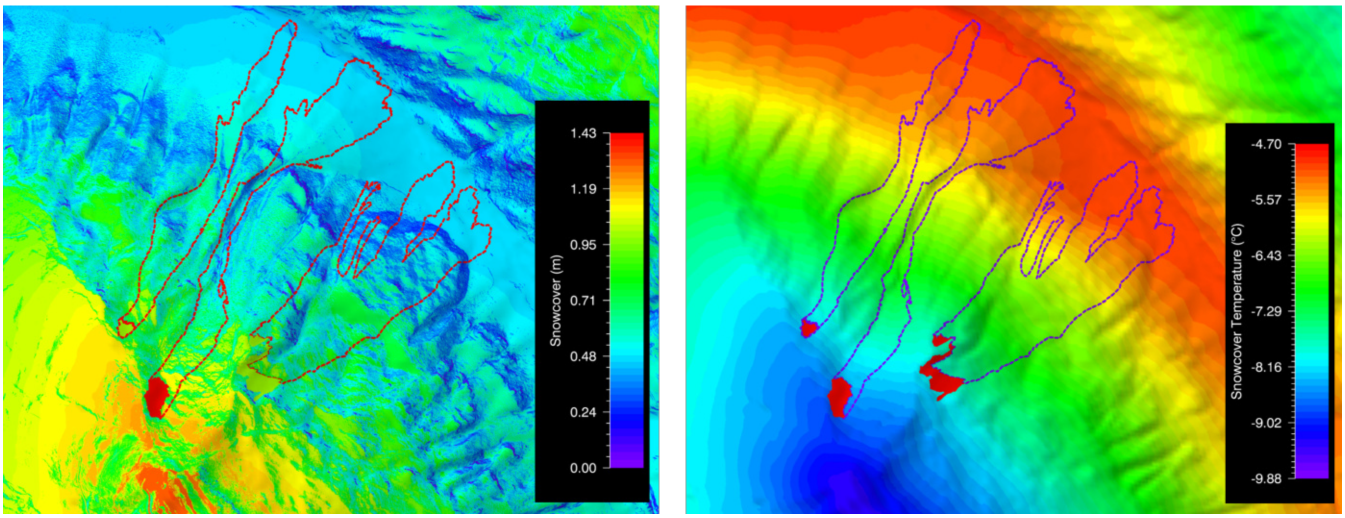

Figure 5. Simulated erodable snow cover (left) and temperature distribution (right) applied for the modelling.

We conducted a sensitivity analysis to determine how well the model represented avalanche behaviour. We started with a local sensitivity analysis, based on the measurements shown in Fig. 2. To fix the input parameter set, we used the weather station data and systematically varied one input parameter at a time, with an emphasis on those parameters which practitioners can measure. The goal of that study was to quantify the impact of uncertainties in input parameters on simulation outcomes. Subsequently, we expanded to varying pairs of parameters, such as snowcover temperature and temperature gradient. Details of these initial findings are discussed in (Glaus et al.).

2.3 A Method to Model Snowcover Distribution $d_\Sigma(Z)$ and Temperature $T_\Sigma(Z)$

The underlying idea behind the Swiss guidelines on avalanche dynamics calculations is to exploit long-term, measured frequency-magnitude data to determine avalanche fracture heights d_0. Avalanche fracture heights are explicitly related to measured, ex-

https://doi.org/10.5194/egusphere-2024-771
Preprint. Discussion started: 22 April 2024

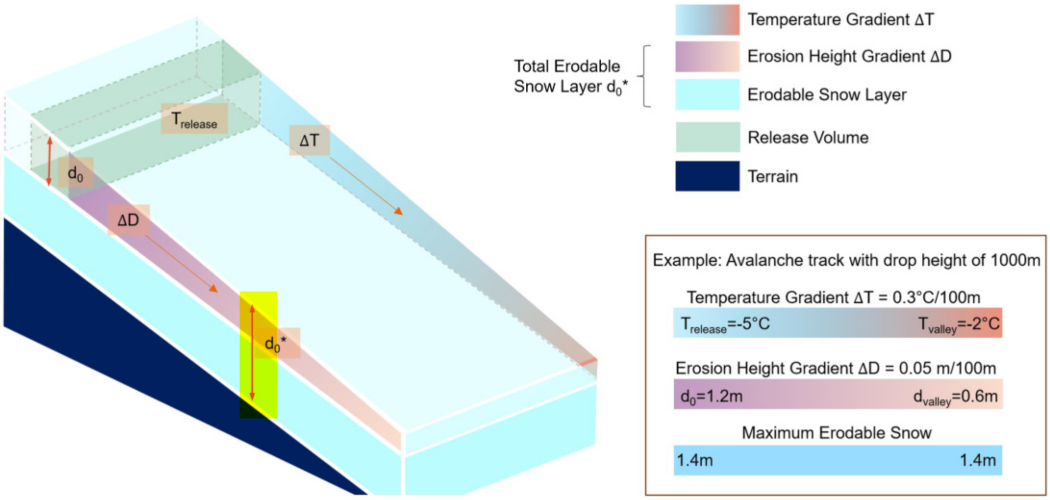

Figure 6. Snowcover temperature and height gradients. The field measurements and weather stations were used to determine average snow-cover height and temperature gradients.

treme three-day new snow accumulation heights (Salm et al., 1990). This procedure underscores two salient assumptions of the Swiss guidelines. Firstly, regional variations in snowfall climatology are included via the measurement data (snow height frequency) and secondly, extreme avalanche activity is directly related to intense new snowfall. In the following we develop a methodology to determine avalanche entrainment heights for road safety calculations within the framework of these existing Swiss guideline procedures, that upholds these two basic assumptions.

Because the snow monitoring stations are located at different elevations and different slope angles, snow accumulation data must be adjusted to account for the specific elevation and slope of the avalanche release zone. Within the guidelines this is performed by applying a snow height gradient ΔD. If Z_m is the elevation of the measurement station, and Z_0 is the elevation of the avalanche release zone, the first iteration of the fracture height $(d_0)^1$ is found by adjusting the value obtained d_m obtained from the statistical frequency-magnitude analysis of the measurement station (Salm et al., 1990),

$$(d_0)^1 = d_m + \Delta D\,(Z_0 - Z_m)\,. \tag{1}$$

The gradient ΔD is expressed in m per 100 m change in elevation, see Fig. 6. Higher snow accumulation heights are found at higher elevations. Typical gradient values for Switzerland (European Alps) are 0.03 m/100 m $\leq \Delta D \leq$ 0.05/100 m (Salm et al., 1990).

The next iteration $(d_0)^2$ accounts for the slope angle of the release zone. The height $(d_0)^1$ is adjusted with the slope reduction factor $f(\psi)$ (Salm et al., 1990)

$$f(\psi) = \frac{0.291}{\sin(\psi) - 0.202\cos(\psi)} \tag{2}$$

https://doi.org/10.5194/egusphere-2024-771
Preprint. Discussion started: 22 April 2024

to calculate avalanche fracture heights,

$$d_0 = (d_0)^2 = f(\psi)(d_0)^1. \tag{3}$$

The slope reduction formula is derived by treating the new snow layer as a Mohr-Coulomb continuum governed by cohesion (c ≈ 600 Pa) and internal friction angle $\tan(\phi)$ = 0.202 with density ρ_0 = 200kg/m^3 (Burkard and Salm, 1992).

We adopt the same two-step procedure to derive entrainment heights for road safety calculations. Moreover, we take

$$d_\Sigma(Z) = f(\psi)\left[d_m + \Delta D\,(Z - Z_m)\right]. \tag{4}$$

where we now replace the fracture zone elevation Z_0 with the slope elevation Z. This procedure thus places less snow on very steep track segments, for example on cliff-faces. In the following we do not take the guideline values for accumulation gradients, but the values derived directly from the measurements ΔD = 0.1 m / 100 m, see Table 1 as described in the chapter 2.

Snowpack simulations have been employed to determine snow temperature and moisture content to assess the onset of wet snow avalanche activity (Wever et al., 2016, 2018; Vera Valero et al., 2018). Here we concerned with cold, dry snowpacks driven by falling air temperatures accompanied by post-storm open skies (negative longwave energy balance). Because of the avalanche tracks are located in close proximity to snow monitoring stations, we take the measurement data to determine the temperature gradient in the snowcover.

In the new snow accumulations strong temperature gradients exist in both the release and run-out zones (see in the Appendix Fig. A1 the snowpit measurements at nearby stations at the altitude of the release zone and deposition). The measurements indicate that low temperatures ($T_m \approx$ -8.5°C) exist in the avalanche release zones (Z = 2300 m), and higher temperatures in the run-out ($T_m \approx$ -2°C). The temperature gradient ΔT = 0.5 °C/100m (Table 1) can be determined from,

$$T_\Sigma(Z) = \left[T_m - \Delta T\,(Z - Z_m)\right]. \tag{5}$$

The gradient ΔT is typically expressed in terms of °C per 100 m change in elevation.

3 Avalanche Model

To simulate the observed avalanches, we utilise the enhanced version of the depth-averaged RAMMS model (Christen et al., 2010). The extended model encompasses the avalanche core (denoted by the Greek letter Φ), the powder cloud (designated as Π), and the underlying snowcover (Σ), see Fig. 7. To accurately model the observed avalanches and snowcover conditions, the following model features are necessary and contained in the extended RAMMS model: (1) Computation of the mean internal energy (thermal temperature) of the avalanche core given the initial temperature of the snowcover. (2) The ability to define snow cover properties as a function of elevation, exposition and slope-dependent terrain features. (3) Track the generation and independent propagation of the powder cloud. Development of the model has been conducted incrementally by Bartelt and Buser, and their collaborators (Bartelt et al., 2006; Buser and Bartelt, 2009a; Bartelt et al., 2012, 2015a, 2018b; Zhuang et al.,

https://doi.org/10.5194/egusphere-2024-771
Preprint. Discussion started: 22 April 2024

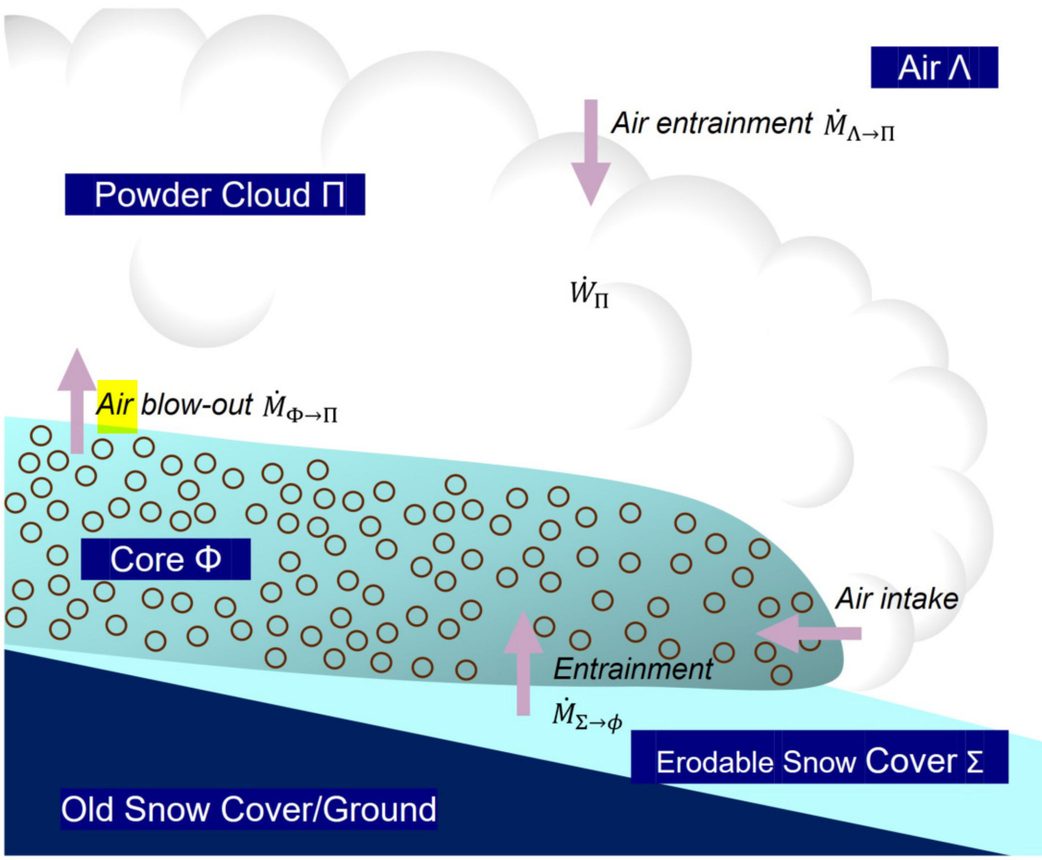

Figure 7. The three primary components of the extended RAMMS model are the avalanche core Φ, the powder cloud Π and the erodible snowcover Σ. The surrounding air is denoted Λ. Mass fluxes (exchanges) are identified:

2023b). Similar models were first developed by Russian researchers (Bozhinskiy and Losev, 1998); however, these models did not include grain flow process physics (Haff, 1983; Hutter et al., 1987; Jenkins and Mancini, 1987; Buser and Bartelt, 2009b) or thermal effects (Vera Valero et al., 2015, 2018). In the following sections, we present the model equations for the core, the cloud and discuss the role of the incumbent snowcover.

3.1 Avalanche core Φ

The avalanche core is a shear flow containing mass in the form of snow clods (grain flow). The core dynamics are characterised by three state variables: namely, the co-volume height $\hat{h}_{\Phi}$, representing the snow packing found in the deposition zone, the dispersed or flowing height h_{Φ}, and the slope-parallel velocity vector $\boldsymbol{u}_{\Phi}$. The co-volume height has the associated density $\hat{\rho}_{\Phi}$, whereas the dispersed flow height has density ρ_{Φ}. The model assumes constant density and velocity profiles. The mass and

https://doi.org/10.5194/egusphere-2024-771
Preprint. Discussion started: 22 April 2024

momentum equations for the avalanche core Φ are,

$$\partial_t \hat{h}_\Phi + \boldsymbol{\nabla}\cdot(\hat{h}_\Phi \boldsymbol{u}_\Phi) = \left[\frac{\rho_\Sigma}{\hat{\rho}_\Phi}\right]\dot{M}_{\Sigma\to\Phi} - \dot{M}_{\Phi\to\Psi} - \left[\frac{\hat{\rho}_\Pi}{\hat{\rho}_\Phi}\right]\dot{M}_{\Phi\to\Pi} \tag{6}$$

$$\partial_t h_\Phi + \boldsymbol{\nabla}\cdot(h_\Phi \boldsymbol{u}_\Phi) = \mathbb{D}(t) \tag{7}$$

$$\partial_t(\hat{h}_\Phi \boldsymbol{u}_\Phi) + \boldsymbol{\nabla}\cdot\left(\hat{h}_\Phi \boldsymbol{u}_\Phi \otimes \boldsymbol{u}_\Phi + p_\Phi I\right) = \boldsymbol{G}\hat{h}_\Phi - \left[\frac{\boldsymbol{u}_\Phi}{||\boldsymbol{u}_\Phi||}\right]\boldsymbol{S}_\Phi - \left[\dot{M}_{\Phi\to\Psi} + \frac{\hat{\rho}_\Pi}{\hat{\rho}_\Phi}\dot{M}_{\Phi\to\Pi}\right]\boldsymbol{u}_\Phi. \tag{8}$$

The avalanche core is driven by gravity $\boldsymbol{G}$ and resisted by shear $\boldsymbol{S}_\Phi$. The mass and momentum balances involve the snowcover entrainment $\dot{M}_{\Sigma\to\Phi}$, forest interaction $\dot{M}_{\Phi\to\Psi}$, and mass/momentum transfer to the cloud $\dot{M}_{\Phi\to\Pi}$. Parameterization of forest detrainment is discussed in detail in (Feistl, 2015). Eq.7 describes the dilution and compression of the core; $\mathbb{D}(t)$ represents the change in core height due to dispersive pressure effects (Buser and Bartelt, 2015), which is found by linking the mass and momentum equations to a grain flow equation for the fluctuation energy (granular temperature) R_Φ, see (Haff, 1983; Jenkins and Savage, 1983; Hutter et al., 1987; Jenkins and Mancini, 1987; Buser and Bartelt, 2009a),

$$\partial_t(\hat{h}_\Phi R_\Phi) + \boldsymbol{\nabla}\cdot(\hat{h}_\Phi R_\Phi \boldsymbol{u}_\Phi) = \alpha_\Phi \dot{W}_\Phi - \dot{M}_{\Phi\to\Pi} R_\Phi - \beta_\Phi \hat{h}_\Phi R_\Phi + \epsilon_\Phi \rho_\Sigma \dot{L}_{\Sigma\to\Phi}. \tag{9}$$

The fluctuation energy R_Φ is associated with random and dispersive particle movements in the flowing granular ensemble is produced by shearing $\dot{W}_\Phi$ (parameter α_Φ) and decaying by collisions/rubbing (parameter β_Φ), see (Haff, 1983; Jenkins and Savage, 1983; Bartelt et al., 2006). Random particle movements are likewise produced during the entrainment process at the rate $L_{\Sigma\to\Phi} = 1/2\dot{M}_\Sigma u_\Phi^2$ (parameter ϵ_Φ), see (Bartelt et al., 2018a). Moreover, snow cannot be entrained in the avalanche without disrupting the mean flow. The counterpart to the macroscopic random fluctuations is identified as another form of stochastic energy, denoted as the internal energy E_Φ, which is the complimentary part of the macroscopic random fluctuations

$$\partial_t(\hat{h}_\Phi E_\Phi) + \boldsymbol{\nabla}\cdot(\hat{h}_\Phi E_\Phi \boldsymbol{u}_\Phi) = [1-\alpha_\Phi]\dot{W}_\Phi - \dot{M}_{\Phi\to\Pi} E_\Phi + \beta_\Phi \hat{h}_\Phi R_\Phi + [1-\epsilon_\Phi]\rho_\Sigma \dot{L}_{\Sigma\to\Phi} + \rho_\Sigma c_\Sigma T_\Sigma \dot{M}_{\Sigma\to\Phi} - \dot{Q}_m - q_{\Phi\to\Lambda}. \tag{10}$$

The model therefore predicts the mean avalanche temperature T_Φ which is related to the internal energy $E_\Phi = \hat{\rho}_\Phi c_\Phi T_\Phi$, where c_Φ is the specific heat capacity of snow at the density ρ_Φ. The term $\dot{Q}_m$ represents the latent heat of melting ice,

$$\int_0^{\Delta t} \dot{Q}_m dt = \rho_i c_i \hat{h}_i [T_i - T_m]. \tag{11}$$

The constant T_m is the melting temperature of ice. The associated change in mass is $\dot{Q}_m/L$ where L is the latent heat of ice. The remaining terms on the right-hand side account for the addition of heat energy from entrained snow and the fraction of heat energy produced during the plastic collision of the snowcover and finally the sensible heat exchange ($q_{\Phi\to\Lambda}$) of the flowing snow with the air. An additional mass balance equation accounts for the intake of bonded water in the snowcover and melting (Valero et al., 2017)

$$\partial_t m_\Phi + \boldsymbol{\nabla}\cdot(m_\Phi \boldsymbol{u}_\Phi) = \frac{\rho_\Sigma}{\rho_w}\eta_w \dot{M}_{\Sigma\to\Phi} + \frac{\dot{Q}_m}{\rho_w L}. \tag{12}$$

The parameter η_w defines the volumetric water fraction in the entrained snow.

https://doi.org/10.5194/egusphere-2024-771
Preprint. Discussion started: 22 April 2024

3.2 Flow friction

The inclusion of the state variables (R_Φ, T_Φ) allows us to define a process based frictional resistance for the avalanche core Φ which is governed by material constants (Table 3.2). We apply a modified Voellmy-type friction law for flowing snow,

$$S_\Phi(R_\Phi) = \mu_\Phi(R_\Phi)N_\Phi + (1-\mu_\Phi(R_\Phi))N_0\left[1-\exp\left(-\frac{N_\Phi}{N_0}\right)\right] + \rho_\Phi g\frac{||\boldsymbol{u}_\Phi||^2}{\xi_\Phi(R_\Phi)} \tag{13}$$

where N_Φ is the basal normal stress; $\mu_\Phi(R_\Phi)$ Coulomb friction; $\xi_\Phi(R_\Phi)$ velocity dependent friction and N_0 the so-called cohesion (Bartelt et al., 2015b). This formula arises directly from chute experiments with flowing snow (Platzer et al., 2007b, a; Bartelt et al., 2015b). When N_0 = 0, the formula collapses to the traditional Voellmy relationship (Salm, 1993). The formula therefore allows us to exploit, if necessary, the long historical knowledge and well-calibrated sets of Voellmy parameters used by practitioners, see (Salm et al., 1990).

The same experiments with flowing snow reveal a strong frictional hysteresis between the front and tail of the flow, indicating a process, or flow dependent relation (Platzer et al., 2007b). Avalanche flow structure, now readily observed in field experiments (Sovilla et al., 2008), is likewise controlled by the frictional hysteresis between front and tail. Moreover, flow resistance at the front of the avalanche differs from the friction at the avalanche tail (Bartelt et al., 2007, 2012). This has significance for the determination of the frictional constants. We note that when R_Φ=0, we have the co-volume, or non-dispersive (dense, plug, tail) friction values $\mu_0 = \mu_\Phi(R_\Phi = 0)$ and $\xi_0 = \xi_\Phi(R_\Phi = 0)$. Lower friction values at the avalanche front are found via,

$$\mu_\Phi(R_\Phi) = \mu_0 \exp\left[-\frac{R_\Phi}{A_\Phi}\right] \qquad \xi_\Phi(R_\Phi) = \xi_0 \exp\left[\frac{R_\Phi}{A_\Phi}\right] \tag{14}$$

where A_Φ is the so-called activation energy (Bartelt et al., 2012). In this model, the avalanche front dynamics, responsible for the formation of the powder cloud, is mathematically represented as the region of the avalanche with higher fluctuation energies R_Φ. The parameters (μ_0, ξ_0, A_Φ) are found via experiments, but more importantly, by back-calculation of measured avalanche deposits (Bartelt et al., 2012). The spatial distribution of avalanche deposits in the field provides the additional needed information to determine friction parameters. For example, they can be immediately estimated in field visits by noting the steepest slope ψ with avalanche snow $\tan(\psi) \approx \mu_0$, as deposition begins when $R_\Phi \to 0$. The location of the frontal deposits (runout) and the terminal velocity of the avalanche are necessary to calibrate the ξ_0 and the activation energy A_Φ. Table 3.2 lists the recommended frictional values we take for avalanching after three-day new snowfall accumulations.

https://doi.org/10.5194/egusphere-2024-771
Preprint. Discussion started: 22 April 2024

Model parameter	Definition	Constant values 3-day snowfall	Thermodynamic constraint	Comment How to determine
μ_0	Coulomb friction (Voellmy, 1955)	μ_0 = 0.55	$\mu_0 > 0$	Controls runout Onset deposition Chute experiments Field observations (Platzer et al., 2007b)
ξ_0	Velocity-squared friction (m/s^2) (Voellmy, 1955)	ξ_0 = 1800	$\xi_0 > 0$	Controls velocity Field experiments (Bartelt et al., 2012) (Zhuang et al., 2023b)
N_0	Cohesion (Pa) (Bartelt et al., 2015b)	N_0 = 200	$N_0 \geq 0$	Controls runout Chute experiments (Bartelt et al., 2015b)
A_Φ	Activation energy (kJ) (Bartelt et al., 2012)	A_Φ=2	$A_\Phi > 0$	Controls spatial distribution avalanche deposits (Bartelt et al., 2012)
α_Φ	Generation R_Φ (-) (Haff, 1983) (Hutter et al., 1987) (Jenkins and Savage, 1983) (Bartelt et al., 2006)	α_Φ=0.07	$0 \leq \alpha_\Phi \leq 1$	Controls flow density (front) Controls avalanche length Powder cloud formation Powder cloud height (Dreier et al., 2016) (Zhuang et al., 2023b)
β_Φ	Decay R_Φ (-) (Haff, 1983) (Hutter et al., 1987) (Jenkins and Savage, 1983) (Bartelt et al., 2006)	$\beta_\Phi(T_\Phi)$ Eq. 15	$\beta_\Phi > 0$	Controls flow density (front) Controls avalanche structure Tail formation Controls spatial distribution avalanche deposits (Bartelt et al., 2012)

For our present purposes to investigate cold, mixed flowing avalanches appearing after new snowfall periods, we will take the model parameters (μ_0, ξ_0, N_0, A_Φ, α_Φ) to be temperature independent constants (Table 3.2). The only temperature dependent parameter will be the decay of fluctuation energy $\beta_\Phi(T_\Phi)$. With the arctangent relationship

$$\beta_\Phi(T_\Phi) = 1.40 + \frac{1.6}{\pi}\arctan(1.6(T_\Phi - 271.5)) \tag{15}$$

https://doi.org/10.5194/egusphere-2024-771
Preprint. Discussion started: 22 April 2024

we ensure that the decay coefficient is within the range 0.6/s $\leq \beta_\Phi \leq$ 2.0/s. As the inverse of β_Φ physically represents the lifetime of the fluctuation energy R_Φ it is linked to the onset of deposition and the flow structure of the avalanche (formation of the avalanche tail). It can therefore be determined by measuring the distribution of deposits in the avalanche runout zone (Bartelt et al., 2012). The lifetime of the fluctuation energy decreases as the avalanche temperature increases; it is approximately four times longer in a cold avalanche than a warm avalanche. This ensures that warm, moist avalanches have plug-like flow regimes (Köhler et al., 2018).

Finally, we presently do not consider the influence of generated meltwater on the frictional constants, assuming that the snow temperature remains below the melting temperature of ice.

3.3 Powder cloud Π

A comparable set of partial differential equations is proposed to model the powder cloud Π. The air-blast is simulated by equations governing mass (Eqs.16 and 17) and momentum balance (Eq. 18), along with supplementary equations related to the generation and dissipation of turbulent fluctuations (Eq.19):

$$\partial_t \hat{h}_\Pi + \boldsymbol{\nabla} \cdot (\hat{h}_\Pi \boldsymbol{u}_\Pi) = \dot{M}_{\Phi\to\Pi} \tag{16}$$

$$\partial_t h_\Pi + \boldsymbol{\nabla} \cdot (h_\Pi \boldsymbol{u}_\Pi) = \dot{M}_{\Lambda\to\Pi} + \left[\frac{\rho_i - \hat{\rho}_\Pi}{\rho_i - \rho_\Lambda}\right] \dot{M}_{\Phi\to\Pi}. \tag{17}$$

$$\partial_t (\hat{h}_\Pi \boldsymbol{u}_\Pi) + \boldsymbol{\nabla} \cdot \left(\hat{h}_\Pi \boldsymbol{u}_\Pi \otimes \boldsymbol{u}_\Pi + p_\Pi \boldsymbol{I}\right) = \left[\frac{\hat{\rho}_\Pi - \rho_\Lambda}{\hat{\rho}_\Pi}\right] \boldsymbol{G}\hat{h}_\Pi + \dot{M}_{\Phi\to\Pi}\boldsymbol{u}_\Pi - \left[\frac{\boldsymbol{u}_\Pi}{||\boldsymbol{u}_\Pi||}\right] \boldsymbol{S}_\Pi - \left[\frac{\rho_\Lambda}{\hat{\rho}_\Pi}\right] \dot{M}_{\Lambda\to\Pi}\boldsymbol{u}_\Pi. \tag{18}$$

$$\partial_t (\hat{h}_\Pi R_\Pi) + \boldsymbol{\nabla} \cdot (\hat{h}_\Pi R_\Pi \boldsymbol{u}_\Pi) = \dot{W}_\Pi + \dot{M}_{\Phi\to\Pi} R_\Phi + \frac{1}{2}\rho_\Lambda \dot{M}_{\Lambda\to\Pi} ||\boldsymbol{u}_\Pi||^2 - \beta_\Pi \hat{h}_\Pi R_\Pi. \tag{19}$$

Analogous to the core, $\hat{h}_\Pi$ represents the initial cloud height, corresponding to the initial cloud density $\hat{\rho}_\Pi$ before expulsion from the core. The variable h_Π denotes the actual cloud height influenced by dust-air mixture expelled from the core $\dot{M}_{\Phi\to\Pi}$ and air entrainment $\dot{M}_{\Lambda\to\Pi}$. Due to this air entrainment, the cloud density decreases to ρ_Π, satisfying $\rho_\Pi = \rho_i \left[\frac{\phi_i \hat{h}_\Pi}{h_\Pi + \phi_i \hat{h}_\Pi}\right] + \rho_\Lambda \left[\frac{h_\Pi}{h_\Pi + \phi_i \hat{h}_\Pi}\right]$, where $\rho_i = 971$ kg/m^3 is the ice density, $\rho_\Lambda = 1.225$kg/m^3 is the air density, and $\phi_i = \left[\frac{\hat{\rho}_\Pi - \rho_\Lambda}{\rho_i - \rho_\Lambda}\right]$ represents the ice fraction in the initial cloud. The cloud is propelled by the momentum imparted from the core $\dot{M}_{\Phi\to\Pi}\boldsymbol{u}_\Phi$ and gravity $\left(\frac{\rho_\Pi - \rho_\Lambda}{\rho_\Pi}\right)\mathbf{G}_\Pi$. Generally, we observe $\dot{M}_{\Phi\to\Pi}\boldsymbol{u}_\Phi \gg \left(\frac{\rho_\Pi - \rho_\Lambda}{\rho_\Pi}\right)\mathbf{G}_\Pi$.

The fluctuation energy is produced by three sources (Eq. 19): internal shearing $W_\Pi = [\hat{\rho}_\Pi S_\Pi]\,||\boldsymbol{u}_\Pi||$, fluctuation energy transferred from the core $\dot{M}_{\Phi\to\Pi} R_\Phi$ and air entrainment $\frac{1}{2}\rho_\Lambda \dot{M}_{\Lambda\to\Pi} u_\Pi^2$. β_Π is the parameter that controls the decay of turbulence, and therefore the lifetime, of the fluctuation energy $-\beta_\Pi \hat{h}_\Pi R_\Pi$. The pressure p_Π includes both the hydrostatic and turbulent parts. More details of the powder model equations, including the entrainment function $\dot{M}_{\Lambda\to\Pi}$, friction $\boldsymbol{S}_\Pi$ and turbulence parameters is contained in the publication (Zhuang et al., 2023b).

https://doi.org/10.5194/egusphere-2024-771
Preprint. Discussion started: 22 April 2024

3.4 Entrainment

Entrainment in the extended model equations is treated as a plastic collision between the avalanche core and the snow cover (Bartelt et al., 2018a). We initially define the mass per unit second $\dot{M}_\Sigma$ that is affected by the passage of the avalanche core:

$$\dot{M}_\Sigma = \kappa_\Sigma \left[\frac{\rho_\Sigma}{\hat{\rho}_\Phi}\right] ||\boldsymbol{u}_\Phi||. \tag{20}$$

We represent this interaction rate as proportional to the avalanche speed $||\boldsymbol{u}_\Phi||$, as it determines the distance the avalanche travels during the interaction time. Avalanches moving at higher speeds cover more ground, leading to an increase in the amount of snow cover mass affected by the avalanche. The dimensionless parameter κ we define as the erodibility coefficient. Essentially, κ determines the depth of the erosion front in the snowcover. Low κ values indicate that only the surface of the snowcover is affected by the avalanche passage (basal erosion), while, conversely, high values of κ indicate that that the core affects the entire depth of the snowcover (frontal erosion). The value of κ can be adjusted to incorporate a bonding strength of the snow μ_b. Defining g_s to be the slope parallel acceleration and g_z as the slope normal acceleration, we modify κ to be,

$$\kappa = \frac{\kappa'}{g}\left[g_s - \mu_b g_z\right] \quad \text{where} \quad \kappa \geq 0 \text{ always.} \tag{21}$$

For 3-day accumulation periods with new snow, we take κ' = 0.015 and $\mu_b \approx 0$. These values ensure that on steep slopes with high avalanche velocities we model frontal entrainment, whereas as on flatter slopes and lower avalanche speeds we enter a mode of basal erosion. The bonding strength model is motivated by observations of eroded segments in avalanche tracks. On track segments where there are no depositions, the eroded snow cover layer can be observed. In this case, the parameter μ_b must be smaller than the tangent of the slope angle.

Presently, $\dot{M}_\Sigma$ represents the snowcover mass affected by the avalanche core – not the total amount of snow taken in by the avalanche. We now partition the affected mass into two parts: a part of mass which is entrained by the avalanche, and a part of the mass which is not entrained, possibly splashed in front of the core to build a pre-front, or frontal saltation layer Γ,

$$\dot{M}_\Sigma = \dot{M}_{\Sigma\to\Phi} + \dot{M}_{\Sigma\to\Gamma} \tag{22}$$

The mass flux $\dot{M}_{\Sigma\to\Phi}$ represents the snowcover mass that is accelerated to the avalanche velocity and can be found on the right and side of model equations Eq. 6 and Eq. 8. We apply a partitioning parameter γ to separate the entrained/non-entrained possibilities of the snowcover interaction,

$$\dot{M}_{\Sigma\to\Gamma} = \gamma \dot{M}_\Sigma \qquad \dot{M}_{\Sigma\to\Phi} = (1-\gamma)\dot{M}_\Sigma \tag{23}$$

The parameter γ, which we term the splashing parameter, could also represent the non-entrained mass in the disrupted snowcover that is simply compacted by the passage of the avalanche front. Obviously, different snowcovers will be governed by different entrainment parameters (κ', μ_b γ). For 3-day new snow accumulation periods we always take γ=0.2.

https://doi.org/10.5194/egusphere-2024-771
Preprint. Discussion started: 22 April 2024

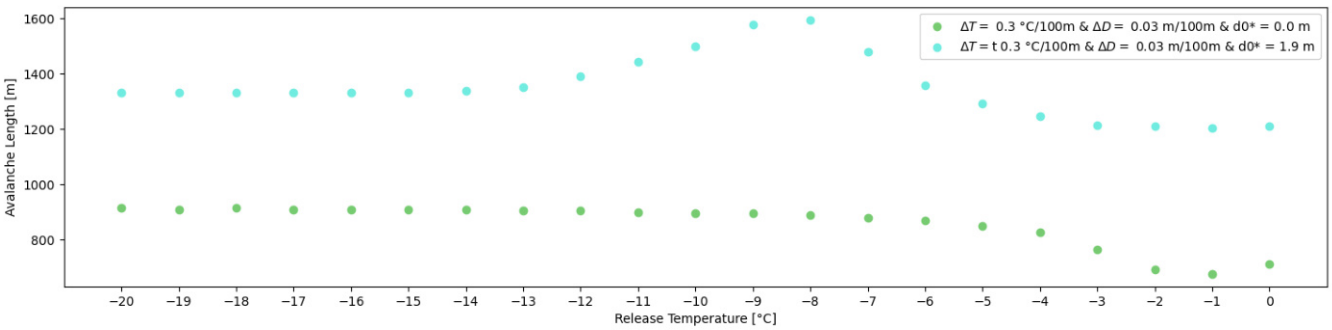

Figure 8. Simulation on a flat surface of an avalanche with different release temperatures changing the influence of erosion. The results of the simulations without erosion sometimes overlap and are hence not visible.

4 Results and Discussion

In the following, we present an analysis on system parameters, particularly friction parameters, to delve deeper into the mathematical model's representation of release temperature (Section 4.1), friction parameters (Section 4.2) and erosion (Section 4.3).

4.1 Snow Temperature

In most avalanching situations, alpine snow is within a few degrees of its phase transition point (T = 0 °C). The physical properties of flowing snow undergo rapid transformations as temperatures edge towards the melting threshold. In the model equations the temperature dependence is contained in the grain flow parameter β (Eq. 15) (Haff, 1983) which describes the decay of the random kinetic energy (granular temperature) and therefore the dispersion of the snow granules. The parameter is set such that colder avalanches exhibit the tendency to form mixed flowing avalanches (Bartelt et al., 2012), while warmer avalanches will exhibit more plug-type flows (Dent et al., 1998). By defining the avalanche release temperature, not only do we set the initial thermal energy, but we also dictate the predisposition of the avalanching snow towards dry, mixed flowing avalanche or moist flow regimes.

In a first series of numerical experiments, we applied the model on an idealized planer slope (Fig. 3). The slope inclination was set to approximate the Breamabühl slopes under investigation. In this way secondary terrain features inducing flow channels and secondary flow figures could be removed from the analysis and model performance gauged in idealized conditions. We varied release temperatures from extremely cold temperatures to zero (-20 °C $\leq T_0 \leq$ 0 °C).

In the first simulations we included no entrainment d_0^*= 0. Therefore, no additional snow was eroded by the avalanche. We calculated the run-out distance according to our post-processing procedure of minimum heights and velocities (green dots, Fig. 8). In this case the run-out distances remained over a wide temperature range (-20 °C $\leq T_0 \leq$ -8 °C). At higher temperatures the grain flow parameter increases with the effect of producing less fluidized flows and shorter run-outs.

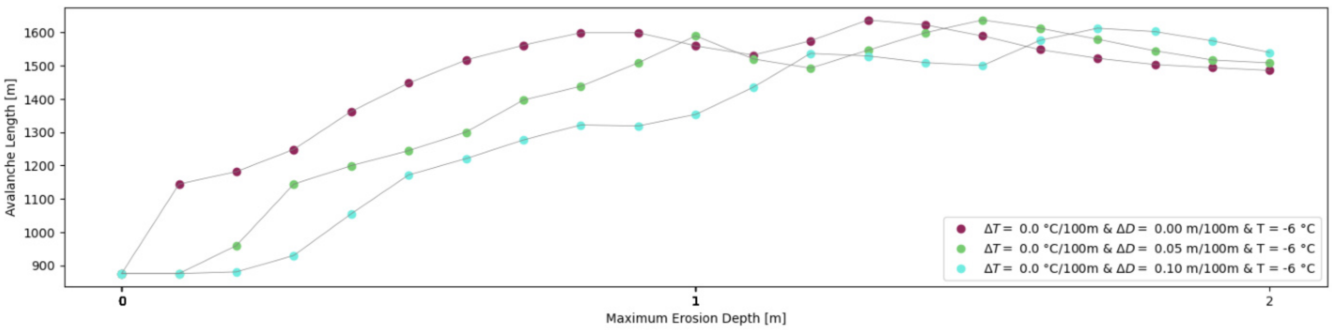

Figure 9. Simulation on a flat surface of an avalanche with different values for the maximum erosion depth for different erosion gradients. For all three curves, there release temperature was fixed at -6 °C and the temperature gradient set to zero, such that the snowcover has everyhwere the same temperature.

By incorporating erosion in our simulations, we add entrained mass to the flowing avalanches and their responses get more intricate. In a subsequent series of simulations we assume a deep snowcover d_0^*= 1.9m with a small height differentials ΔD = 0.03 m / 100 m and temperature gradients ΔT = 0.3 °C / 100 m (blue dots, Fig. 8). At extremely cold temperatures -20 °C $\leq T_0 \leq$ -10 °C the calculated run-out distances remain stable. The reason for this behaviour is the grain flow parameter β. For very cold avalanches, the formation of the powder cloud dominates, extracting mass and energy from the core, ultimately leading to dispersion and dissipation of the avalanche. As the temperatures increase, an optimal balance between the core and cloud emerges, yielding far-reaching flows. With the specification of more realistic release temperatures, $T > -10$ °C the run-out distances increase. This phenomenon underscores the counteracting effects of frictional heating (rise in temperature) and the entrainment of cold snow (decrease in temperature). The avalanche temperature remains lower for longer, fostering long enduring fluidized regimes and more potent powder avalanches. The model predicts that the entrainment of cold snow at lower elevations facilitates the fluidized regime and the formation of powder avalanches. However, the run-out distances decrease again with higher release and entrainment conditions T_0 = -8°C (Fig. 8). At higher temperatures the decay of fluctuation energy increases, leading to dense, less fluidized flows and therefore an increase in friction which curbs run-out distances. It becomes evident that the temperature dependent grain flow parameter, $\beta(T_\Phi)$ controls the flow regime of the calculated avalanches with and without entrainment.

In the next series of simulations on the idealized planar slope , we vary the snow height gradient ΔD = 0.0, 0.05 and 0.10m/100m; the release temperature remains set at T_0= -6C and the temperature gradient is zero ΔT = 0. Less snow is subsequently encountered by the avalanche at lower elevations in the run-out zone. We perform simulations with different values of snow heights 0.0 m $\leq d_0^* \leq$ 2.0 m. This situation mirrors actual snow conditions in road safety applications in which the snow distribution represents the largest uncertainty. We simulate the difference between shallow and deep snow covers with different height gradients.

The results indicate that for shallow snowcovers $d_0^* \leq$ 1.0m, the different gradients produced large differences in avalanche run-out (Fig. 9). Avalanches that encounter snow along the entire track (ΔD = 0.0 m / 100 m) run longer than when they

https://doi.org/10.5194/egusphere-2024-771
Preprint. Discussion started: 22 April 2024

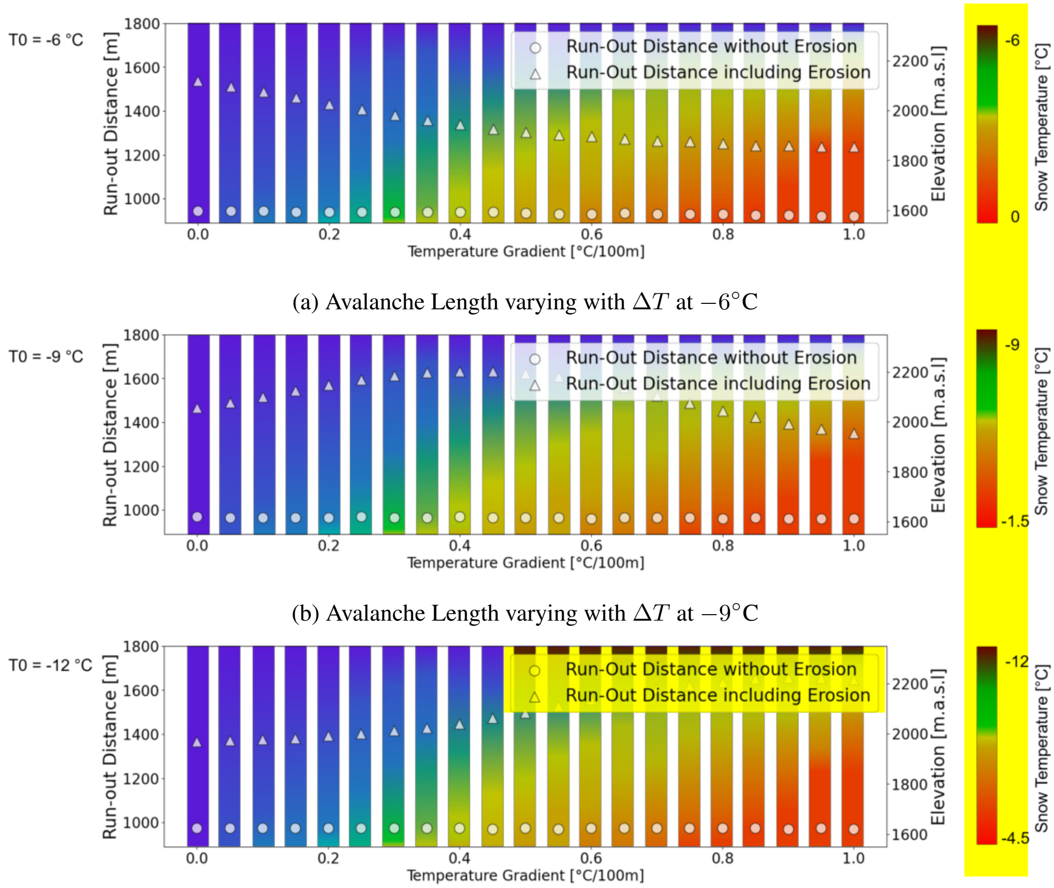

(a) Avalanche Length varying with ΔT at $-6°$C

(b) Avalanche Length varying with ΔT at $-9°$C

(c) Avalanche Length varying with ΔT at $-12°$C

Figure 10. Simulation of avalanche run-out on the idealized planar slope with and without erosion. We consider three initial temperatures (a) T_0 = -6°C (b) T_0 =-9°C and (c) T_0 = -9°C for variable temperature gradients ΔT. The colors on the blocks depict the temperature gradients varying from cold snow (blue) to warm snow (red). The results indicate the reduction in avalanche run-out as a cold avalanche runs into a warm snowcover. The colder the initial temperature the less the reduction.

encounter regions of no snow in the run-out zone. This results corresponds well with experience that a deep snowcover from
340 initiation to run-out is needed for extreme avalanche events, especially powder snow avalanches. For the case of $d_0^* > 1.0$ m, the gradients appear to have no influence on the avalanche run-out. The snow is so deep, that gradients play a subordinate role in determining the avalanche danger.

Another useful depiction of the simulation results is shown in Fig. 10. In this figure we plot the decrease in avalanche run-out for variable temperature gradients ΔT as we simulated it on the idealized planar slope. The colors on the blocks depict the
345 temperature gradients varying from cold snow (blue) to warm snow (red) as a function of the run-out distance. The simulations are performed for three initial release temperatures (a) T_0 = -6°C (b) T_0 = -9°C and (c) T_0 = -12 °C. The results indicate the

https://doi.org/10.5194/egusphere-2024-771
Preprint. Discussion started: 22 April 2024

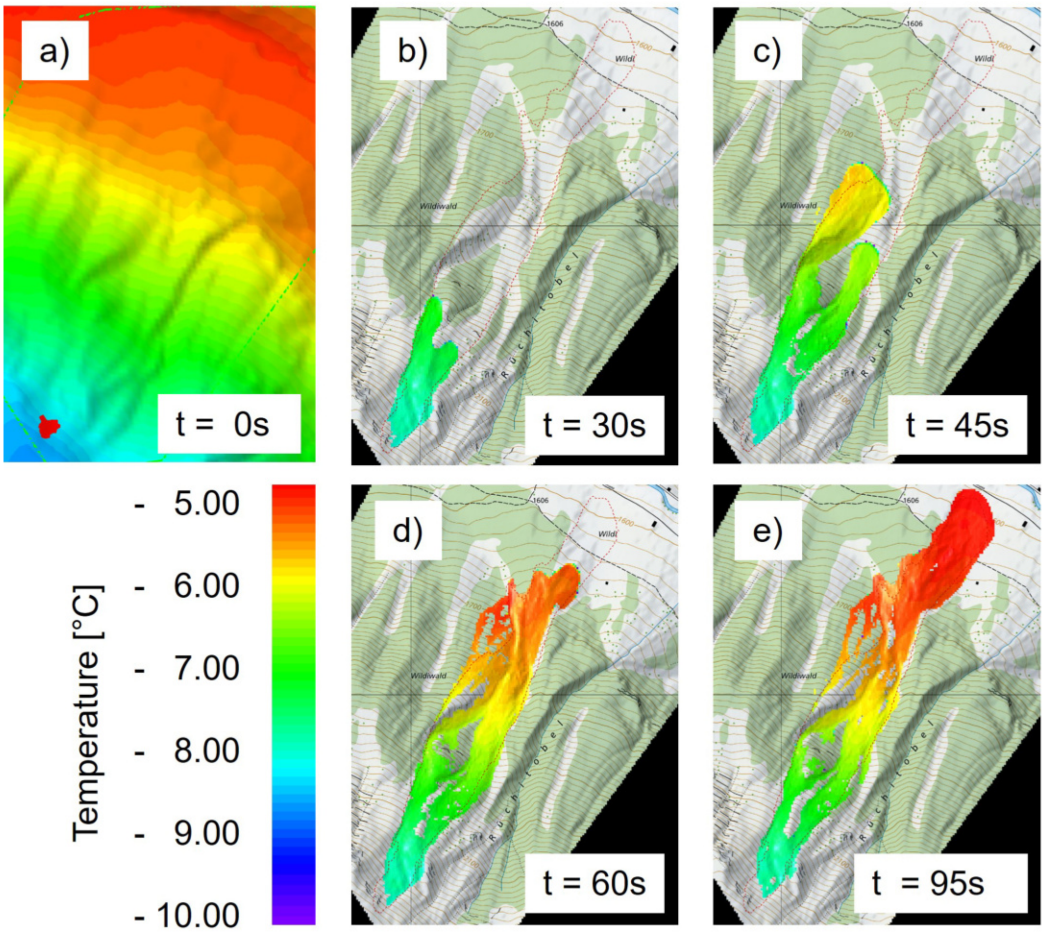

Figure 11. Evolution of temperature in the Wildi avalanche over time, t = 0s (a) to t = 95s (e). Inset (a) depicts the initial temperature of the snow cover (map source: Federal Office of Topography).

reduction in avalanche run-out as a cold avalanche runs into a warm snowcover. The colder the initial temperature the less the reduction. The results underscore the complex interplay between erosion and avalanche temperature.

The simulations on the idealized planar slope are useful because they highlight the role of the initial snowcover temperature and temperature gradient on the avalanche flow regime and run-out distance without terrain effects. On a actual slope the snowcover height is not only given by the elevation gradient ΔD but also the local slope inclination. The simulated evolution of avalanche temperature over time for the case Wildi avalanche is depicted in Fig. 12. The initial temperatures are specified using the weather station and snowpit data. This figure displays the calculated mean avalanche temperature T_Φ of the avalanche core, which increases from T_Φ = -8°C to T_Φ = -5°C in the run-out zone. Moreover, a ΔT_Φ = 3°C change in avalanche temperature is predicted. The calculated avalanche temperature represents a competition between the increase produced by the frictional

https://doi.org/10.5194/egusphere-2024-771
Preprint. Discussion started: 22 April 2024

shearing rate (which is dependent the avalanche velocity and therefore terrain) and the snow intake (Valero et al., 2015). The model equations assume that the entrained snow mixes with the avalanche snow instantaneously, producing a new mean temperature. In reality, the energy exchange between the avalanche snow and the entrained snow will take time. Temperature variations will exist in the avalanche; heat concentrations will most likely exist on the surface of the granules, while the interior of the granules remains cold(Jomelli and Bertran, 2004; Steinkogler et al., 2015).

4.2 Friction Parameters μ_0, ξ_0, N_0

In the preceding section all the calculations were performed with constant friction and process parameters (see Table 3.2) representing avalanche situations governed by periods of new snowfall. The simulation results indicate that given an initial release location, mass and temperature, the calculated terminal velocity and avalanche run-out are governed by snowcover disposition and temperature. Traditionally run-out and velocity are reproduced in avalanche dynamics calculations by changing the values of the friction parameters from avalanche to avalanche creating an envelope of extreme values(Gruber and Bartelt, 2007). Here, we do not adopt this approach. Friction parameters dynamically change as a function of temperature according to the process chain,

$$T_\Phi(t) \rightarrow R_\Phi(t) \rightarrow \text{Voellmy parameters}\,[\mu(t), \xi(t)]\,. \tag{24}$$

This chain of relationships indicates that the temperature of snow influences the mean fluctuation energy (via the decay parameter $\beta(T_\Phi)$, which controls the dispersion of snow granules and therefore avalanche flow regime. This fluctuation energy, being a stochastic variable, signifies the inherent randomness in the movement of all granules within the flowing snow ensemble relative to the mean. The momentary state of friction is influenced by this fluctuation energy. Thus, the basic model assumption is that the temperature of snow governs the stochastic dynamics of its granular ensemble, ultimately impacting frictional behavior. The grain flow process parameters controlling the relationship between $R_\Phi(t)$ and flow friction (avalanche deposition) have been identified by (Bartelt et al., 2012) in the study of Vallée de la Sionne avalanches.

It is now necessary to validate this approach using the Braemabuel avalanches using the measured drone data and weather station input. For this the initial values of the friction parameters μ_0 and ξ_0 were varied to identify the combination which results in the measured avalanche run-out distance. This was also done for different cohesion values. The results are depicted in Fig. 12. For some cohesion values, the measured run-out distance could not be reproduced. Therefore, we restricted the investigated cohesion values to the range obtained from measurements conducted in snow chutes (Bartelt et al., 2012).

We find that the best-fit to the avalanche run-out distance is provided by friction values $0.55 \leq \mu_0 \leq 0.50$ and 1750m/s^2 $\leq \xi_0 \leq$ 2200m/s^2 in good agreement with values found in Vallée de la Sionne (Bartelt et al., 2012). The range of ξ_0 parameters could be reduced by knowing the avalanche velocity. In Figure 12, the Ruechi Tobel exhibits the most symmetric pattern in terms of friction values. This is attributed to the fact that the Ruechi Tobel features a straightforward avalanche outline without any flow fingers.

https://doi.org/10.5194/egusphere-2024-771
Preprint. Discussion started: 22 April 2024

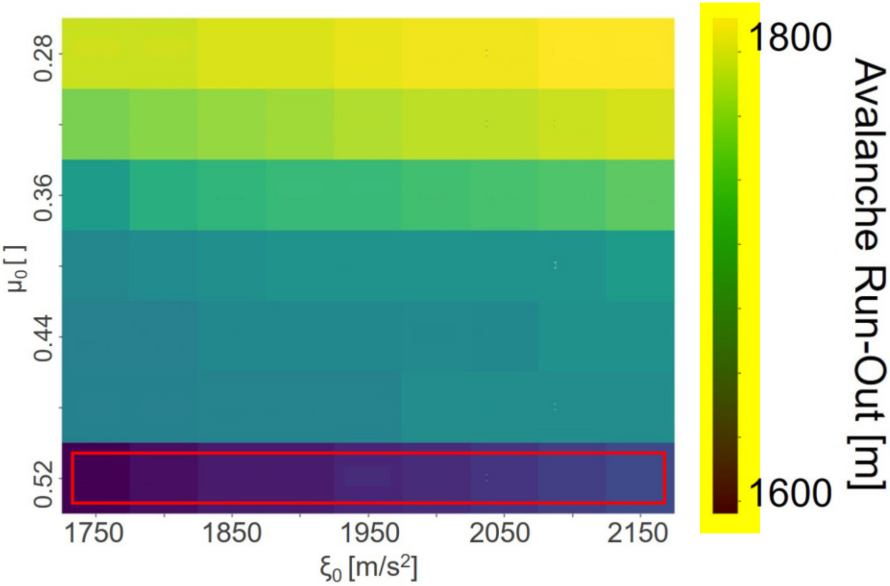

Figure 12. Simulation of the Ruechi avalanche with different friction values and a cohesion of N_0=150 Pa. The measured run-out length plus minus 5 percent error (over and underprediction of the avalanche run-out) is marked by the red squares. The best-fit parameters are near the recommended values in Table 3.2

4.3 Comparison to Measured Avalanches

The determination of the optimal friction parameters in the preceding section uses only the observed run-out distance. However, the drone data and photo data provide much useful information. Most importantly, the observed lateral flow width of the avalanche, avalanche volume and the height and travel distance of the powder cloud can be ascertained.

Fig. 13 depicts the calculated extent of the model avalanches in comparison to the measured outlines. Of significance is the relatively good agreement between the calculated and measured avalanche flow width.

Each avalanche was accompanied by a powder cloud that ran-up the counter slope (Fig. 15). The calculated powder cloud widths are in good agreement with the observations. We estimate the maximum powder cloud heights reached up to 40 m, comparing the photographs of the fully developed powder cloud with the tree heights know from a LiDAR based vegetation height model; maximum air-blast pressures on the road never exceeded 5 kPa. Regions of isolated tree damage by the powder cloud are reproduced by the model.

In Fig. 16, the snow height in the deposition of the Ruechi is compared to the simulated deposition height. The depiction of the measured snow height shows the evolution of deposited avalanche arms. Particularly on the right side in the flow direction of the avalanche, a stronger arm has formed, which is also evident in the simulation. The total snow volume present in the area overflown by the avalanche in Fig. 16 is approximately 155000 m^3, measured by the photogrammetric snow depth mapping

https://doi.org/10.5194/egusphere-2024-771
Preprint. Discussion started: 22 April 2024

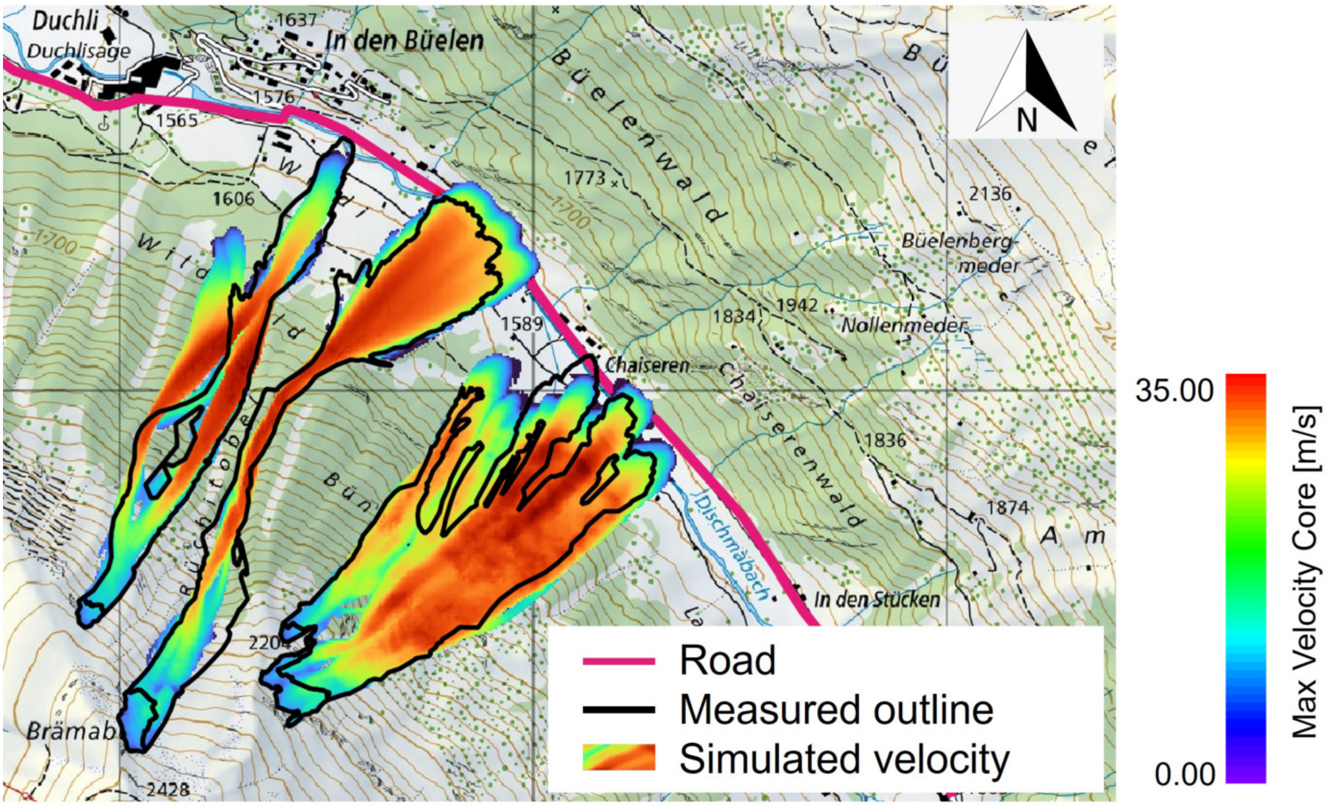

Figure 13. Comparison of the measured outlines of the Braemabuel avalanches with the model results using the measured snowcover height and temperature data (map source: Federal Office of Topography).

with the drone. The simulated deposition in the same area is only approximately $30000m^3$. The drone measurements assess the total volume of snow present an the acquisition time. As the avalanche ran on an an already present snow cover of approximately 1 m (measured next to the avalanche deposit, resulting in a already present volume of approximately $100000m^3$), this is the main explanation for the difference. Furthermore a large part of the deposition in the simulated avalanche is already deposited further up in the avalanche track and the front part of the deposition is stopping just outside of the mapped avalanche outline and is therefore not taken into account for the volume calculation. The depositions simulated in the upper part of the track are also present in the drone measurements and the simulations at similar locations Fig. 13 and show similar deposition heights.

The drone orthophoto of the Chaiseren avalanche track showed that its snowpack had been scoured by wind, resulting in less accumulated snow than was calculated by the snow gradients used in our simulations. Therefore, the initial snow mass is over-estimated in this simulation.

https://doi.org/10.5194/egusphere-2024-771
Preprint. Discussion started: 22 April 2024

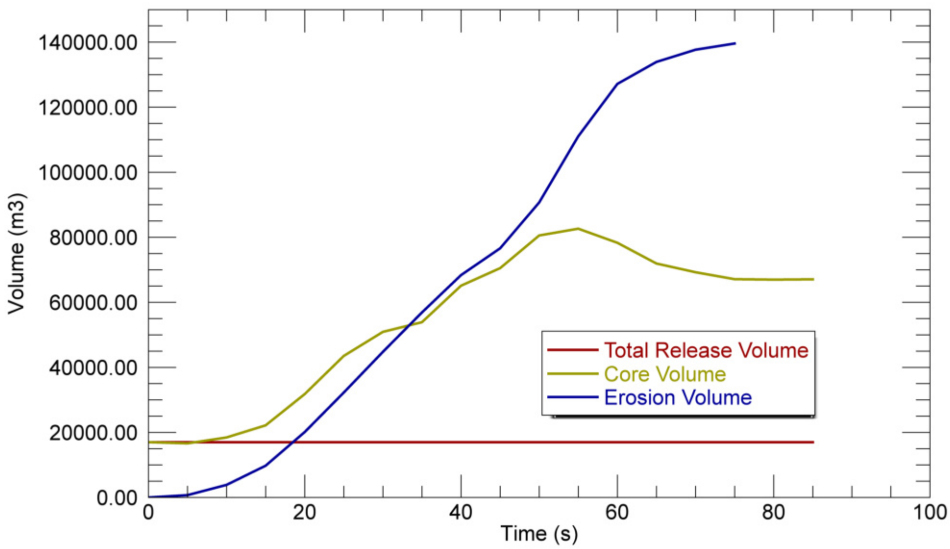

Figure 14. Evolution of avalanche volume for the Braemabühl avalanche for the Ruechi track.

5 Conclusion

For road safety management it is essential to estimate the run-out of avalanches potentially reaching sections of the road, based on near real time weather and snowpack conditions. To support these decisions, we tested an avalanche dynamics model to simulate the run-out distance of cold powder avalanches including the impact pressures of the powder cloud, which is often the most relevant danger for cars and people. To do so, incorporating erosion and the influence of temperature distribution across the erodible snowpack is essential. Additionally, differing flow regimes, e.g. avalanches which start in a cold snowpack (< -5°C average) runing into a warmer snowpack (-5°C to -1°C) could be taken into account.

The applied model continues to utilise a Voellmy-based frictional approach as in the well-established models applied for hazard mapping. However, the friction coefficients are now dynamically calculated and are affected by terrain and snowpack variables, which differ considerably between different avalanche tracks and avalanche periods. To set up the simulations we apply snowpack parameters measured at nearby automated weather stations and snow profiles. To validate the results, we apply photogrammetrically measured snow depth distributions acquired by drones, capturing the extreme spatial variability of snow depth distribution in mountain terrain very accurately.

The results demonstrate that we are able to simulate avalanches based on measurements at weather stations such as snow height and snow temperature at different altitudes and locations to calculated the snow cover distribution and snow temperature gradient. Choosing weather stations from a nearby valley (pproximately 3 km distance) showed acceptable results with a coefficient of variation below 5 %. Comparing the modelled avalanche outlines to the measured ones, it is visible, how the

https://doi.org/10.5194/egusphere-2024-771
Preprint. Discussion started: 22 April 2024

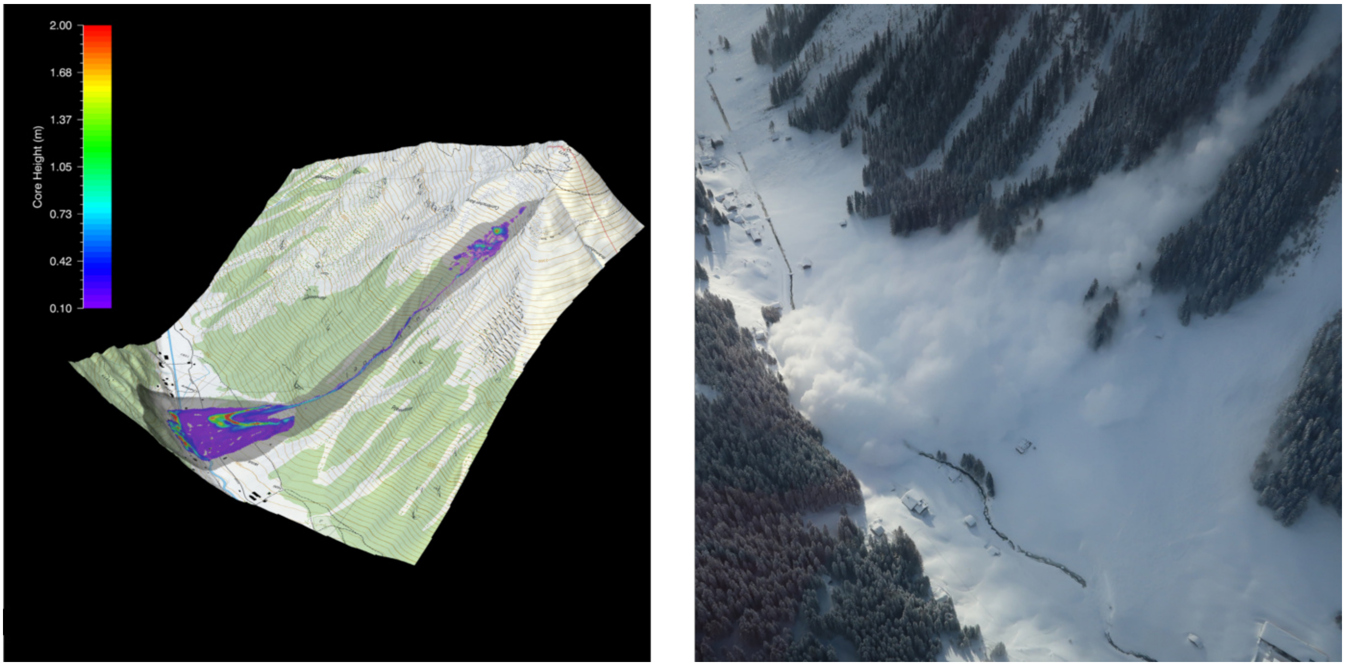

Figure 15. Simulation of the powder cloud accompanying the Ruechi avalanche (left) simulation and (right) photo of the cloud taken from the helicopter (map source: Federal Office of Topography).

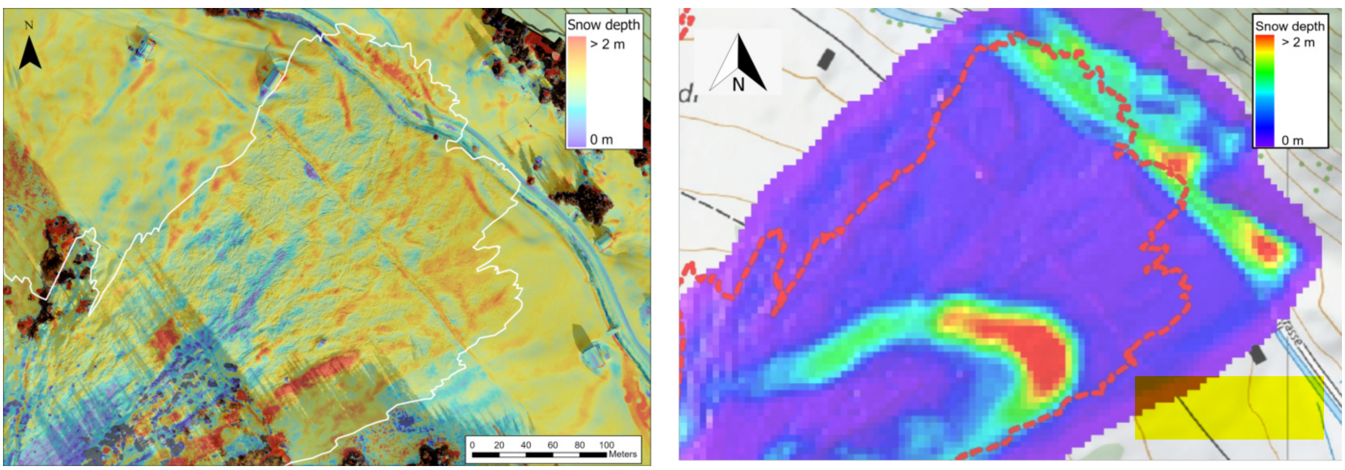

Figure 16. Comparison of the deposition area of the measured (left) and modelled (right) Ruechi Tobel avalanche (map source: Federal Office of Topography).

model represents important features such as the evolution of fingers indicating zones with higher impact pressures or the development of the powder cloud.

https://doi.org/10.5194/egusphere-2024-771
Preprint. Discussion started: 22 April 2024

As nearby and representative weather station measurements are not accessible for many roads, in a next step, snow cover models as SNOWPACK (Lehning et al., 1999) and CROCUS (Vionnet et al., 2011) could be used to calculated the relevant input parameters. For rough estimations of the snow temperature, it would be necessary to compare the cloud coverage during the hours before the avalanche occurred to the average temperature of the release snow mass. As the run-out distance is not too sensitive to the input temperature, a first approach could be to define simulation scenarios of cold and warm temperatures depending on the cloud coverage. To enable the model to simulate additional wet snow avalanches, we need to collect more avalanche data that is directly related to measured snowpack temperature and moisture content. Potentially releasing avalanche starting zones have to be defined by the experts prior to the simulations. This is an important source of uncertainty. A first approach could be to use automatically delineated release areas as proposed by (Bühler et al., 2022, 2018).

The presented approach will now be applied to calculate avalanche run-out for different representative weather and snowpack scenarios for the Dischma road. These results will then be validated by the local experts and and the applicability of this approach for future decision making will be assessed. A probabilistic approach is currently being tested to calculate reach probabilities to the road for specific avalanche tracks. These are important steps towards a more data-based decision making for road management in mountain regions.

https://doi.org/10.5194/egusphere-2024-771
Preprint. Discussion started: 22 April 2024

Acknowledgements. This research is funded by the Swiss National Science Foundation (SNSF) under project number 207519, titled "Avalanche Safety for Roads". The authors express their gratitude to SOS Davos Klosters for their collaboration and provision of avalanche run-down pictures.

Author contributions. Study design: YB, PB and JG, Expert protective measures: LS, Technical implementation: MC, Data processing: KWJ, with inputs from AV, AW and YB, Manuscript: PRJ with contributions from all co-authors

Competing interests. At least one of the (co-)authors is a member of the editorial board of Natural Hazards and Earth System Sciences.

Financial support. This research is funded by the Swiss National Science Foundation SNSF with the project "Avalanche Safety for Roads" (Nr. 207519).

Data availability. The post processing tool and the used data for the mapped avalanche outlines will be available on GitHub and EnviDat on the publication of the final script.

https://doi.org/10.5194/egusphere-2024-771
Preprint. Discussion started: 22 April 2024

455 # Appendix

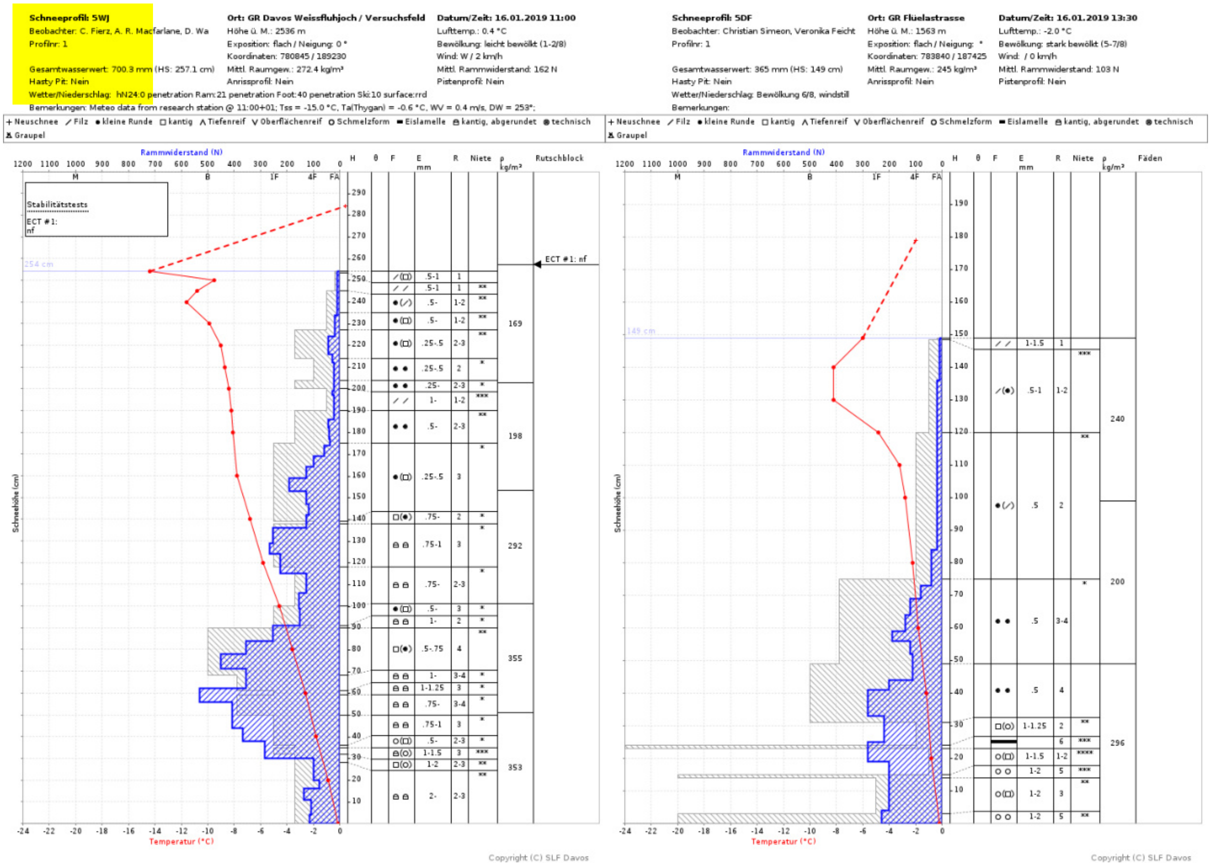

Figure A1. Snowpit data for the station at Weissfluhjoch and at SLF Davos (Source: https://whiterisk.ch produced by SLF).

https://doi.org/10.5194/egusphere-2024-771
Preprint. Discussion started: 22 April 2024

References

AvaFrame, https://doi.org/10.5281/zenodo.8319432, supplement to: https://github.com/avaframe/AvaFrame/tree/1.6.1, 2023.

Ammann, W. J.: A new Swiss test-site for avalanche experiments in the Vallée de la Sionne/Valais, Cold Regions Science and Technology, 30, 3–11, https://doi.org/10.1016/S0165-232X(99)00010-5, 1999.

Bartelt, P., Buser, O., and Platzer, K.: Fluctuation-dissipation relations for granular snow avalanches, Journal of Glaciology, 52, 631–643, 2006.

Bartelt, P., Buser, O., and Platzer, K.: Starving avalanches: frictional mechanisms at the tails of finite-sized mass movements, Geophysical Research Letters, 34, 1–6, https://doi.org/10.1029/2007GL031352, 2007.

Bartelt, P., Bühler, Y., Buser, O., Christen, M., and Meier, L.: Modeling mass-dependent flow regime transitions to predict the stopping and depositional behavior of snow avalanches, Journal of Geophysical Research, 117, F01 015, 2012.

Bartelt, P., Buser, O., Valero, C., and Bühler, Y.: Configurational energy and the formation of mixed flowing/powder snow and ice avalanches, Annals of Glaciology, 57, 179 – 188, https://doi.org/10.3189/2016AoG71A464, 2015a.

Bartelt, P., Valero, C., Feistl, T., Christen, M., Bühler, Y., and Buser, O.: Modelling cohesion in snow avalanche flow, Journal of Glaciology, 61, 837 – 850, https://doi.org/10.3189/2015JoG14J126, 2015b.

Bartelt, P., Christen, M., Bühler, Y., Caviezel, A., and Buser, O.: Snow Entrainment: Avalanche interaction with an erodible substrate, in: Proceedings, International Snow Science Workshop, pp. 16–720, 2018a.

Bartelt, P., Christen, M., Bühler, Y., Caviezel, A., and Buser, O.: Snow entrainment: avalanche interaction with an erodible substrate, International Snow Science Workshop Proceedings 2018, Innsbruck, pp. 716 – 720, 2018b.

Bozhinskiy, A. N. and Losev, K.: The fundamentals of avalanche science, https://www.dora.lib4ri.ch/wsl/islandora/object/wsl%3A17257/, iSSN: 0415-0759, 1998.

Brabec, B. and Meister, R.: A nearest-neighbor model for regional avalanche forecasting, Annals of Glaciology, 32, 130–134, https://doi.org/10.3189/172756401781819247, 2001.

Burkard, A. and Salm, B.: Die Bestimmung der mittleren Anrissm ¨achtigkeit d0 zur Berechnung von Fliesslawinen, Tech. rep., SLF, Davos, Switzerland, 1992.

Buser, O. and Bartelt, P.: Production and decay of random kinetic energy in granular snow avalanches, Journal of Glaciology, 55, https://doi.org/10.3189/002214309788608859, 2009a.

Buser, O. and Bartelt, P.: Production and decay of random kinetic energy in granular snow avalanches, Journal of Glaciology, 55, 3–12, https://doi.org/10.3189/002214309788608859, 2009b.

Buser, O. and Bartelt, P.: An energy-based method to calculate streamwise density variations in snow avalanches, Journal of Glaciology, 61, 563–575, 2015.

Bühler, Y., Christen, M., Kowalski, J., and Bartelt, P.: Sensitivity of snow avalanche simulations to digital elevation model quality and resolution, Annals of Glaciology, 52, 72 – 80, https://doi.org/10.3189/172756411797252121, 2011.

Bühler, Y., Adams, M., Stoffel, A., and Bösch, R.: Photogrammetric reconstruction of homogenous snow surfaces in alpine terrain applying near-infrared UAS imagery, International Journal of Remote Sensing, 38, https://doi.org/10.1080/01431161.2016.1275060, 2017.

Bühler, Y., Rickenbach, D., Stoffel, A., Margreth, S., Stoffel, L., and Christen, M.: Automated snow avalanche release area delineation-validation of existing algorithms and proposition of a new object-based approach for large-scale hazard indication mapping, Natural Hazards and Earth System Sciences, 18, 3235–3251, https://doi.org/10.5194/nhess-18-3235-2018, 2018.

Bühler, Y., Bebi, P., Christen, M., Margreth, S., Stoffel, L., Stoffel, A., Marty, C., Schmucki, G., Caviezel, A., Kühne, R., and Wohlwend, S.: Automated avalanche hazard indication mapping on a statewide scale, Natural Hazards and Earth System Sciences, 22, 1825 – 1843, https://doi.org/10.5194/nhess-22-1825-2022, 2022.

Cerda, P., Gallardo, L. A., Didier, M., Joaquin, M. O., Rodrigo, M. F., and Vera, C.: Avalanche Management in a Large Chilean Copper Mine, https://api.semanticscholar.org/CorpusID:133105900, 2016.

Christen, M., Kowalski, J., and Bartelt, P.: RAMMS: Numerical simulation of dense snow avalanches in three-dimensional terrain, Cold Regions Science and Technology, 63, 1–14, https://doi.org/10.1016/j.coldregions.2010.04.005, 2010.

Dent, J., Burrell, K., Schmidt, D. S., Louge, M., Adams, E., and Jazbutis, T.: Density, velocity and friction measurements in a dry-snow avalanche, Annals of Glaciology, 26, 247–252, https://doi.org/10.3189/1998AoG26-1-247-252, 1998.

Dreier, L., Bühler, Y., Ginzler, C., and Bartelt, P.: Comparison of simulated powder snow avalanches with photogrammetric measurements, Annals of Glaciology, 57, https://doi.org/10.3189/2016AoG71A532, 2016.

Feistl, T.: Forest damage and snow avalanche flow regime, Natural Hazards and Earth System Sciences, 15, https://doi.org/10.5194/nhess-15-1275-2015, 2015.

Glaus, J., Wikstrom-Jones, K., Buehler, Y., Christen, M., Ruttner-Jansen, P., Gaume, J., and Bartelt, P.: RAMMS::EXTENDED – Sensitivity Analysis OF Numerical Fluicized Powder Avalanche Simulationin Three-Dimensional Terrain.

Gruber, U. and Bartelt, P.: Snow avalanche hazard modelling of large areas using shallow water numerical methods and GIS, Environmental Modelling and Software, 22, 1472–1481, https://doi.org/10.1016/j.envsoft.2007.01.001, 2007.

Haff, P. K.: Grain flow as a fluid-mechanical phenomenon, Journal of Fluid Mechanics, 134, 401–430, 1983.

Hutter, K., Szidarovszky, F., and Yakowitz, S.: Granular shear flows as models for flow avalanches, IAHS Publ., 162, 381–394, symposium at Davos 1986-Avalanche Formation, Movement and Effects, 1987.

Jenkins, J. T. and Mancini, F.: Plane flows of a dense, binary mixture of smooth, nearly elastic circular disks, Journal of Applied Mechanics, 54, 27–34, 1987.

Jenkins, J. T. and Savage, S. B.: A theory for the rapid flow of identical, smooth, nearly elastic particles, Journal of Fluid Mechanics, 136, 186–202, 1983.

John, S.: I-90 Snoqualmie Pass: Operating a Highway Avalanche Program During a Major Construction Project, https://api.semanticscholar.org/CorpusID:55292369, 2012.

Jomelli, V. and Bertran, P.: Wet Snow Avalanche Deposits in the French Alps: Structure and Sedimentology, Geografiska Annaler: Series A, Physical Geography, 83, 15 – 28, https://doi.org/10.1111/j.0435-3676.2001.00141.x, 2004.

Keiler, M., Sailer, R., Jörg, P., Weber, C., Fuchs, S., Zischg, A. P., and Sauermoser, S.: Avalanche risk assessment - A multi-temporal approach, results from Galtuer, Austria, Natural hazards and earth system sciences, https://doi.org/10.5194/nhess-6-637-2006, 2006.

Köhler, A., Fischer, J. T., Scandroglio, R., Bavay, M., Mcelwaine, J., and Sovilla, B.: Cold-to-warm flow regime transition in snow avalanches, The Cryosphere Discussions, pp. 1–22, https://doi.org/10.5194/tc-2018-67, 2018.

Lehning, M., Bartelt, P., Brown, B., Russi, T., Stöckli, U., and Zimmerli, M.: SNOWPACK model calculations for avalanche warning based upon a network of weather and snow stations, Cold Regions Science and Technology, 30, 145–157, https://doi.org/10.1016/S0165-232X(99)00022-1, 1999.

Platzer, K., Bartelt, P., and Jaedicke, C.: Basal shear and normal stresses of dry and wet snow avalanches after a slope deviation, Cold Regions Science and Technology, 49, 11–25, https://doi.org/10.1016/j.coldregions.2007.04.003, 2007a.

https://doi.org/10.5194/egusphere-2024-771
Preprint. Discussion started: 22 April 2024

Platzer, K., Bartelt, P., and Kern, M.: Measurements of dense snow avalanche basal shear to normal stress ratios (S/N), Geophysical Research Letters, 34, L07 501, 2007b.

Rauter, M., Kofler, A., Huber, A., and Fellin, W.: FaSavageHutterFOAM 1.0: Depth-integrated simulation of dense snow avalanches on natural terrain with OpenFOAM, Geoscientific Model Development, 11, 2923–2939, https://doi.org/10.5194/gmd-11-2923-2018, 2018.

Salm, B.: Flow, flow transition and runout distances of flowing avalanches, Annals of Glaciology, 18, 221–226, https://doi.org/10.3189/s0260305500011551, 1993.

Salm, B., Burkard, A., and Gubler, H. U.: Berechnung von Fliesslawinen. Eine Anleitung fuer Praktiker mit Beispielen, vol. 47 of *Mitteilungen des Eidg. Institutes für Schnee- und Lawinenforschung*, Eidgenössisches Institut für Schnee- und Lawinenforschung, Weissfluhjoch/-Davos, 1990.

Sovilla, B., Schaer, M., Kern, M., and Bartelt, P.: Impact Pressures and flow regimes in dense snow avalanches observed at the Valle de la Sionne test site, Journal of Geophysical Research, 113, https://doi.org/10.1029/2006JF000688, 2008.

Steinkogler, W., Gaume, J., Löwe, H., Sovilla, B., and Lehning, M.: Granulation of snow: From tumbler experiments to discrete element simulations, Journal of Geophysical Research: Solid Earth, 120, https://doi.org/10.1002/2014JF003294, 2015.

Stoffel, L. and Schweizer, J.: Guidelines for avalanche control services: organization, hazard assessment and documentation – an example from Switzerland, pp. 483–489, 2008.

Swisstopo: Swiss Federal Office of Topography (swisstopo), https://www.swisstopo.admin.ch/, accessed: March 8, 2024.

Valero, C., Wikstrom J., K., Bühler, Y., and Bartelt, P.: Release temperature, snow-cover entrainment and the thermal flow regime of snow avalanches, Journal of Glaciology, 61, 173 – 184, https://doi.org/10.3189/2015JoG14J117, 2015.

Valero, C., Wever, N., Christen, M., and Bartelt, P.: Modeling the influence of snowcover temperature and water content on wet snow avalanche runout, Natural Hazards and Earth System Sciences Discussions, pp. 1–32, https://doi.org/10.5194/nhess-2017-36, 2017.

Vera Valero, C., Wikstroem Jones, K., Bühler, Y., and Bartelt, P.: Release temperature, snow-cover entrainment and the thermal flow regime of snow avalanches, Journal of Glaciology, 61, 173–184, https://doi.org/10.3189/2015JoG14J117, 2015.

Vera Valero, C., Wever, N., Bühler, Y., Stoffel, L., Margreth, S., and Bartelt, P.: Modelling wet snow avalanche runout to assess road safety at a high-altitude mine in the central Andes, Natural Hazards and Earth System Sciences, 16, 2303–2323, https://doi.org/10.5194/nhess-16-2303-2016, 2016.

Vera Valero, C., Wever, N., Christen, M., and Bartelt, P.: Modeling the influence of snow cover temperature and water content on wet-snow avalanche runout, Natural Hazards and Earth System Sciences, 18, 869–887, https://doi.org/10.5194/nhess-18-869-2018, 2018.

Vionnet, V., Brun, E., Morin, S., Boone, A., Faroux, S., Le Moigne, P., Martin, E., and Willemet, J.-M.: The detailed snowpack scheme Crocus and its implementation in SURFEX v7, Geoscientific Model Development Discussions, 4, https://doi.org/10.5194/gmdd-4-2365-2011, 2011.

Voellmy, A.: Über die Zerstörungskraft von Lawinen, https://doi.org/10.5169/seals-61878, 1955.

Wever, N., Vera Valero, C., and Fierz, C.: Assessing wet snow avalanche activity using detailed physics based snowpack simulations, Geophysical Research Letters, 43, 5732–5740, https://doi.org/10.1002/2016GL068428, 2016.

Wever, N., Vera Valero, C., and Techel, F.: Coupled snow cover and avalanche dynamics simulations to evaluate wet snow avalanche activity, Journal of Geophysical Research F: Earth Surface, 123, 1772–1796, https://doi.org/10.1029/2017JF004515, 2018.

Zhuang, Y., Piazza, N., Xing, A., Christen, M., Bebi, P., Bottero, A., and Bartelt, P.: Tree blow-down by snow avalanche air-blasts: dynamic magnification effects and turbulence, Geophysical Research Letters, 50, e2023GL105 334, https://doi.org/10.1029/2023GL105334, 2023a.

https://doi.org/10.5194/egusphere-2024-771
Preprint. Discussion started: 22 April 2024

Zhuang, Y., Xing, A., Bartelt, P., Bilal, M., and Ding, Z.: Dynamic response and breakage of trees subject to a landslide-induced air blast, Natural Hazards and Earth System Sciences, 23, 1257–1266, https://doi.org/10.5194/nhess-23-1257-2023, 2023b.